Calibration of the Advanced X-ray Astrophysics Facility (AXAF): Project Science analyses

M. C. Weisskopf
NASA, Marshall Space Flight Center, ES01

R. F. Elsner, S. L. O'Dell, M. E. Sulkanen, and A. F. Tennant
NASA, Marshall Space Flight Center, ES84

R. A. Austin, J. J. Kolodziejczak, D. A. Swartz, and G. Zirnstein
USRA, Marshall Space Flight Center, ES84

Preliminary report

1997 October 17

Abstract

This document is the preliminary report on Project Science analyses of data from the calibration of the Advanced X-ray Astrophysics Facility (AXAF). The report provides an introduction to AXAF calibration activities at the X-Ray Calibration Facility (XRCF) and then describes Project Science analyses of calibration data:

1. Beam-Normalization Detector (BND) data for X-ray Source System (XSS) monochromators;
2. Solid-State Detector (SSD) internal calibrator;
3. Solid-State Detector (SSD) continuum measurements;
4. Flight Contamination Monitor (FCM); and
5. Limits on High-Resolution Mirror Assembly (HRMA) contamination.

Contents

1 Introduction **1**
1.1 Calibration instrumentation at the XRCF . . . 1
1.1.1 X-ray Source System (XSS) . . . 1
1.1.2 Beam-Normalization Detectors (BNDs) . . . 2
1.1.3 X-ray optics . . . 3
1.1.4 Objective transmission gratings . . . 3
1.1.5 Focal-plane detectors . . . 3
1.2 Calibration activities at the XRCF . . . 4
1.2.1 Calibration phases . . . 4
1.2.2 Observatory calibration timeline . . . 5
1.3 Project Science analyses . . . 5
1.3.1 BND data for XSS monochromators . . . 6
1.3.2 SSD internal calibrator . . . 6
1.3.3 SSD continuum measurements . . . 6
1.3.4 Flight Contamination Monitor (FCM) . . . 6
1.3.5 Limits on HRMA contamination . . . 6

2 BND data for XSS monochromators **7**
2.1 Objectives . . . 7
2.2 Measurement descriptions . . . 7
2.2.1 Monochromators . . . 7
2.2.2 Flow Proportional Counters (FPCs) . . . 8
2.2.3 Raw data . . . 9
2.3 Data analysis procedures . . . 10
2.3.1 Data acquisition and preprocessing . . . 10
2.3.2 Spectral content . . . 13
2.3.3 Spatial Content . . . 13
2.3.4 Convolution of spectral and spatial information . . . 14
2.4 Results . . . 15
2.5 Data Products . . . 21
2.5.1 Intermediate Products . . . 21
2.5.2 rdb tables . . . 21

3 SSD internal calibrator **24**
3.1 Objectives . . . 24
3.1.1 Gain and energy scale . . . 24
3.1.2 Icing . . . 24
3.2 Procedures . . . 28
3.3 Status . . . 32
3.4 Data products . . . 32

4 SSD continuum measurements **33**
4.1 Effective area . . . 33
4.1.1 Objectives . . . 33
4.1.2 Procedures . . . 33
4.1.3 Status . . . 35
4.1.4 Data products . . . 36
4.2 Alignment . . . 36
4.2.1 Objectives . . . 36
4.2.2 Procedures . . . 36

5 Flight Contamination Monitor **42**
5.1 Objectives . . . 42
5.2 Procedures . . . 42
5.2.1 Source characterization . . . 42
5.2.2 Forward Contamination Cover (FCC) registration . . . 42
5.2.3 Spectral content . . . 42
5.2.4 Contamination and flux scale . . . 42
5.3 Status . . . 43
5.3.1 Source characterization . . . 43
5.3.2 Forward Contamination Cover (FCC) registration . . . 43
5.3.3 Spectral content . . . 44
5.3.4 Contamination and flux scale . . . 44
5.4 Data products . . . 49
5.4.1 Source characterization . . . 49
5.4.2 Forward Contamination Cover (FCC) registration . . . 49
5.4.3 Spectral content . . . 49
5.4.4 Contamination and flux scale . . . 49

6 Limits on HRMA contamination **50**
6.1 Objectives . . . 50
6.1.1 Molecular contamination . . . 50
6.1.2 Particulate contamination . . . 50
6.2 Procedures . . . 50
6.2.1 Molecular contamination . . . 50
6.2.2 Particulate contamination . . . 50
6.3 Status . . . 50
6.3.1 Molecular contamination . . . 50
6.3.2 Particulate contamination . . . 50
6.4 Data products . . . 51

List of Figures

1 X-ray calibration instrumentation at the XRCF 1
2 Schematic of the DCM-RAS7 monochromator. 8
3 Schematic of the HIREFS-RAS14 monochromator. 9
4 Adopted FPC quantum efficiency. 10
5 Representative FPC data and model fits for monochromators. 16
6 Bi-spectrogram for a DCM energy scan. 17
7 Representative DCM beam-uniformity maps. 18
8 Peak-to-valley spatial variations for the DCM. 19
9 Peak-to-valley spatial variations for the HIREFS. 19
10 Estimated fractional error in DCM flux for detector FPC_HT. 20
11 Estimated fractional error in HIREFS flux for detector FPC_HT. 20
12 Flux and estimated fractional error in W-Mα line for detector FPC_HT. 21
13 Temporal dependence of model gain and gain offset parameters. 25
14 Temporal dependence of model gain parameter for restricted data set. 25
15 Temporal dependence of model resolution parameters. 26
16 Temporal dependence of modeled strengths for several lines. 26
17 Temporal dependence of modeled strengths for Fe-K lines. 27
18 Temporal dependence of modeled strengths for Fe-L and O-K lines. 27
19 Spectrum of ^{244}Cm source obtained with SSD_5. 30
20 Low-energy spectrum of ^{244}Cm source obtained with SSD_5. 30
21 Spectrum near Fe-K lines of ^{244}Cm source, obtained with SSD_5. 31
22 Medium-energy spectrum of ^{244}Cm source obtained with SSD_5. 31
23 High-energy spectrum of ^{244}Cm source obtained with SSD_5. 32
24 SSD-measured, primarily continuum spectra for a carbon target at 15 kV. 34
25 Comparison of measured with predicted effective area of each HRMA shell. 35
26 Schematic of HRMA and its XRCF shutter assembly. 36
27 Dependence of shell-6 quadrant-throughput ratio upon off-axis angle. 37
28 Quadrant-throughput ratio for extreme off-axis measurements with shells 1, 3, and 4. . . . 38
29 Measured dependence of shell-6 N/S PHA ratio upon yaw. 39
30 Measured dependence of shell-6 T/B PHA ratio upon pitch. 39
31 Measured N/S PHA ratios at extreme yaw values for shells 1, 3, and 4. 40
32 Comparison of measured and fitted PHA ROI ratios. 41
33 Simulated focal-plane image of FCM, with outlines of AXAF detector focal planes. 43
34 Comparison of simulated and measured HRC-I images of FCM. 45
35 Comparison of centroid of measured HRC-I FCM image with those of simulated images. . 46
36 ACIS image of FCM, in detector coordinates, from Day 116. 46
37 Detected FCM spectrum in ACIS BI CCD S3 amplifier 0, from Day 116. 47
38 Detected FCM spectrum in ACIS FI CCD S2 amplifier 0, from Day 116. 47
39 Detected FCM Ag-L spectrum in ACIS FI CCD S2 amplifier 0, from Day 116. 48
40 Detected FCM Mn-K spectrum in ACIS FI CCD S2 amplifier 0, from Day 116. 48

List of Tables

1 XRCF configurations for the AXAF calibration. 5
2 Timeline for AXAF calibration measurements at the XRCF. 5
3 DCM beam-uniformity maps outside CMDB 11
4 HIREFS beam-uniformity maps outside CMDB 12
5 DCM parameters 12
6 Average FCM activities (mCi) per source for 1997 March 5. 43
7 FCM (Ag-L$\alpha\beta\gamma$/Mn-Kα) count-rate ratios (all grades) for active ACIS CCD amplifiers . 44

1 Introduction

This document is Project Science's contribution to the preliminary report on the calibration of AXAF. Each AXAF Science Instrument team has provided a preliminary report on the calibration analyses for which it is responsible. In order to facilitate the reading of this document, as well as the other documents comprising the full preliminary report, we begin by giving an overview [1] of XRCF calibration instrumentation (§1.1) and of XRCF calibration activities (§1.2). We then summarize those calibration analyses for which Project Science is responsible (§1.3), which is the subject of this document.

1.1 Calibration instrumentation at the XRCF

The X-Ray Calibration Facility (XRCF), operated by MSFC's System Analysis and Integration Laboratory (SAIL), provides a 518-m guide tube separating the x-ray-source building from the Instrument Chamber (IC). For a table of relevant distances and their estimated errors, for configurations used during the calibration of AXAF at the XRCF, please visit the Project Science calibration page at `http://wwwastro.msfc.nasa.gov/xray/xraycal/`.

In this section, we describe x-ray instrumentation, both ground-support and flight, used during AXAF testing and calibration at the XRCF. Figure 1 illustrates the x-ray components employed during the calibration — namely, the source system (§1.1.1), the monitor detectors (§1.1.2), the x-ray optics (§1.1.3), the transmission gratings (§1.1.4), and the focal-plane detectors (§1.1.5).

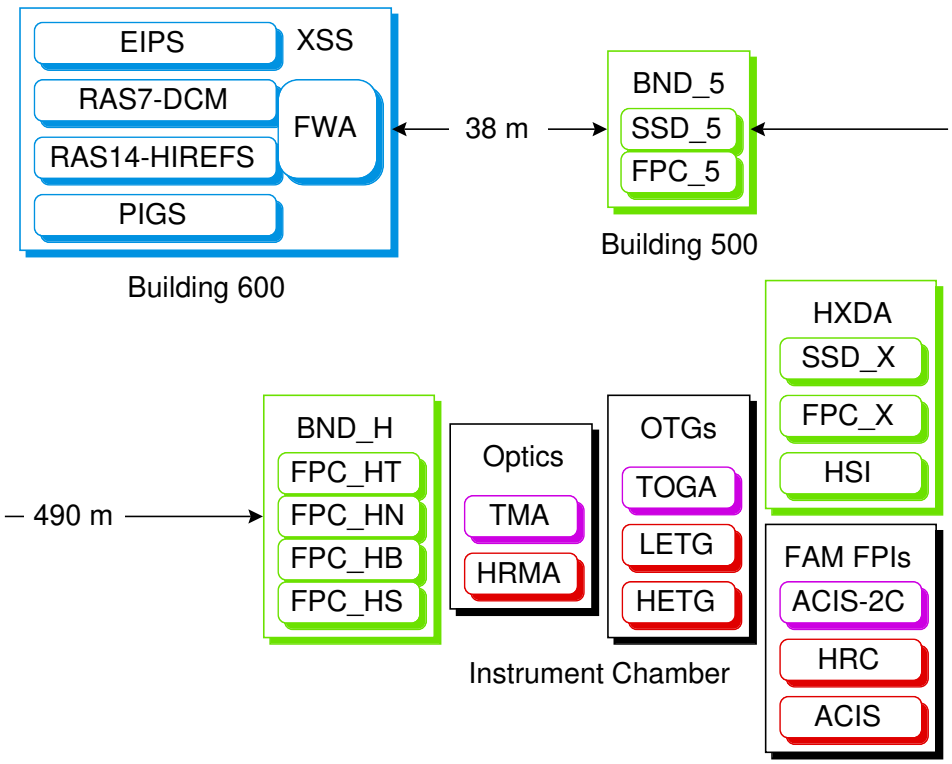

Figure 1: Configurations of x-ray sources, monitor detectors, optics, transmission gratings, and focal-plane detectors during calibration of the AXAF observatory at the X-Ray Calibration Facility (XRCF).

1.1.1 X-ray Source System (XSS)

The X-ray Source System (XSS) [2] comprises a conventional electron-impact source, two monochromators, a Penning source, and transmission filters. MSFC SAIL integrated the XSS; AXAF Project

Science characterized the XSS prior to AXAF calibration. In addition to the x-ray sources of the XSS, the AXAF optics and both focal-plane instruments employ flight, radioactive calibration sources to ensure an accurate ground-to-orbit transfer of the AXAF flux scale [3].

Electron-Impact Point Source (EIPS) MSFC's System Analysis and Integration Laboratory (SAIL) developed the Electron-Impact Point Source (EIPS), which produces electron-induced fluorescence lines and bremsstrahlung in its fixed, oil-cooled anode. Numerous interchangeable, conical-anode targets provide atomic K and L lines over the AXAF energy range (0.1–10 kev).

Double-Crystal Monochromator (DCM) The National Institute of Standards and Technology (NIST) fabricated the dual-pentagonal-turret Double-Crystal Monochromator (DCM). The AXAF calibration employed Thallium Acid Phthalate (TAP001), germanium (Ge111), and abraded silicon (aSi400) crystals to span the respective energy ranges 0.7–2.3, 2.1–8.5, and 6–12 keV. Rigaku manufactured the Rotating Anode Source (RAS) used with the DCM.

Reflection-grating monochromator (HIREFS) Hettrick Scientific fabricated the reflection-grating monochromator, the HIgh-Resolution Erect Field Spectrometer (HIREFS^{TM}). The AXAF calibration employed 3 of the HIREFS' 4 selectable gratings to span the respective energy ranges 0.12–0.40, 0.30–1.2, and 0.9–2.0 keV. Rigaku manufactured the Rotating Anode Source (RAS) used with the HIREFS.

Penning Ionization Gas-discharge Source (PIGS) The Smithsonian Astrophysical Observatory (SAO) Mission Support Team (MST) provided the Penning Ionization Gas-discharge Source (PIGS); MSFC SAIL refurbished the PIGS during the calibration. The PIGS produces narrow, soft-x-ray L lines of ionized aluminum and argon, for calibrating spectral resolution of the AXAF gratings in the energy range 0.07–0.25 keV (wavelengths 170–50 Å).

Filter-Wheel Assembly (FWA) MSFC's System Analysis and Integration Laboratory (SAIL) developed a dual-wheel Filter-Wheel Assembly (FWA), which holds assorted x-ray transmission filters, pin holes, occulting bars, and open (unobstructed) apertures. Nominally, the filters provide 2, 4, or (when used in combination) 6 mean-free-path attenuation at the characteristic lines of EIPS anode targets.

1.1.2 Beam-Normalization Detectors (BNDs)

The Smithsonian Astrophysical Observatory (SAO) Mission Support Team (MST) provided the HRMA X-ray Detection System (HXDS) [4], which comprises Beam-Normalization Detectors (BNDs) to monitor the x-ray source and (non-flight) focal-plane detectors (§1.1.5) to characterize x-ray optics (§1.1.3) and gratings (§1.1.4). Of the 6 BNDs, one is a Solid-State Detector (SSD) and the other 5 are Flow Proportional Counters (FPCs).

Solid-State Detector (SSD) The BND SSD ("SSD_5"), residing approximately 38 m from the XSS (§1.1.1), is a liquid-nitrogen-cooled, high-purity-germanium (hpGe) detector [5]. In front of the detector's 6-mm-diameter active area, lies an aperture wheel, holding circular apertures up to 5-mm diameter and a radioactive calibration source. Prior to the AXAF calibration, SAO and Physikalisch–Technische Bundesanstalt (PTB) calibrated [6] this SSD at the Berliner Elektronenspeicherring-Gesellschaft für Synchrotronstrahlung (BESSY).

Flow Proportional Counters (FPCs) One BND FPC ("FPC_5") lies slightly in front of the BND SSD (SSD_5), about 38 m from the XSS (§1.1.1). This BND, FPC_5, has an aperture slide, with aperture diameters of 1, 4, 12, and 36 mm; it is mounted on a 2-degree-of-freedom stage, for mapping the x-ray beam. Four BND FPCs ("FPC_H") reside just in front of the x-ray optic, about 526 m from the source; one of these is mounted on a 2-degree-of-freedom stage for mapping the x-ray beam near the optic's entrance aperture. SAO and PTB will calibrate the absolute efficiencies of the FPCs at BESSY.

1.1.3 X-ray optics

Calibration activities at the XRCF involved not only the flight optic, the High-Resolution Mirror Assembly (HRMA), but a non-flight optic, the Technology Mirror Assembly (TMA).

High-Resolution Mirror Assembly (HRMA) The Eastman Kodak Company (EKC) aligned and assembled the HRMA; Hughes Danbury Optical Systems (HDOS) figured and polished its Zerodur mirrors; and Optical Coatings Laboratories Inc. (OCLI) sputter-coated the optical surfaces with iridium. With 4 Wolter-1 mirror shells (segment lengths of 0.83 m and diameters of 0.63, 0.85, 0.97, and 1.2 m), the HRMA [7, 8] provides both high-resolution (sub-arcsecond) imaging and a large (1140 cm^2) geometric area. With a focal length of 10 m, the HRMA focal-plane plate scale is about 50-μm/arcsec. EKC provided HRMA ground-support equipment, including actuators to yaw and pitch the HRMA for off-axis measurements and a 16-shutter assembly to isolate specific HRMA mirror-shell quadrants.

Technology Mirror Assembly (TMA) The TMA is a gold-coated 60%-scale model of the smallest of the AXAF's 4 mirror shells. Fabricated and tested a decade earlier, as a demonstration of technologies to be used in producing the mirrors for AXAF, the TMA served as a surrogate optic during calibration rehearsals, prior to arrival of the (flight) HRMA.

1.1.4 Objective transmission gratings

Located immediately behind an optic, objective transmission gratings (OTGs) disperse the convergent beam, to form high-resolution spectra near the focal plane. The AXAF observatory has 2 OTGs — the Low-Energy Transmission Grating (LETG) and the High-Energy Transmission Grating (HETG) — either of which may be inserted into the x-ray path behind the HRMA. Matched to the TMA's geometry, the custom-built TMA Objective Grating Assembly (TOGA), using flight-type gratings from the LETG and the HETG, allowed a realistic rehearsal prior to the HRMA's arrival at the XRCF.

Low-Energy Transmission Grating (LETG) Designed and fabricated by the Space Research Organization of the Netherlands (SRON) and the Max-Planck-Institut für extraterrestrische Physik (MPE), the LETG comprises 540 16-mm-diameter free-standing-gold facets, mounted (3 per module) on a ring structure which locates the facets on the Rowland toroid which includes the focal plane. The Low-Energy Grating (LEG), free-standing gold bars of about 991-nm period, provide high-resolution spectroscopy from 0.08 keV to 2 keV.

High-Energy Transmission Grating (HETG) Designed and fabricated by the Massachusetts Institute of Technology (MIT), the HETG comprises 336 25-mm-square polyimide-supported-gold facets, mounted (1 per frame) on a ring structure which locates the facets on the Rowland toroid. The HETG functions as 2 gratings with slightly rotated dispersion directions: Medium-Energy Gratings (MEG), with a 400-nm period, lie behind the HRMA's outer 2 mirror shells, for high-resolution spectroscopy from 0.4 keV to 4 keV; High-Energy Gratings (HEG), with a 200-nm period, lie behind the inner 2 shells, for high-resolution spectroscopy from 0.8 keV to 8 keV.

TMA Objective Grating Assembly (TOGA) The Massachusetts Institute of Technology (MIT) designed and fabricated the TOGA for use with the TMA. Employing all 3 flight-type grating facets (LEG, MEG, HEG), oriented with different dispersion directions, the TOGA provided early diagnostic data on each type of grating, and the opportunity to rehearse spectroscopy data collection and analysis.

1.1.5 Focal-plane detectors

The AXAF observatory has 2 focal-plane science instruments — the (microchannel plate) High-Resolution Camera (HRC) and the AXAF CCD Imaging Spectrometer (ACIS). Each provides two detectors: The "I" detector is primarily fro direct imaging; the "S" detector is primarily for reading out dispersed spectra of the LETG or of the HETG.

Prior to arrival of the HRC and ACIS at the XRCF, the rehearsal and the HRMA calibration employed 4 non-flight focal-plane detectors. Three of these — an SSD, an FPC, and the (microchannel plate) High-Speed Imager (HSI) — are part of the HRMA X-ray Detector Assembly (HXDA), which also incorporates a 3-degree-of-freedom stage, an SSD aperture wheel, and an aperture plate for the FPC. The SAO Mission Support Team (MST) provided the HXDA, which, with the (monitor) BNDs (§1.1.2), comprise the HRMA X-ray Detection System (HXDS). In addition, the (non-flight) ACIS two chip (ACIS-2C) served as a surrogate CCD detector, to provide practice in CCD data collection and analysis and to calibrate its flight-type CCDs. Ball Aerospace and Technologies designed and fabricated the Five-Axis Mount (FAM) which positioned the ACIS-2C, as well as the HRC and ACIS.

High-Resolution Camera (HRC) The Smithsonian Astrophysical Observatory designed and fabricated the HRC [9]. The HRC-I and HRC-S employ 6°-chevron pairs of low-noise microchannel plates (MCPs), coated with cesium–iodide (CsI) and covered with an aluminized-polyimide UV/ion shield. For both HRC-I and HRC-S, the spatial resolution is better than 20 μm ($<$ 0.4 arcsec) and the read-out resolution is 6.4 μm (0.13 arcsec). With a 93-mm-square active area, HRC-I has a 31-arcmin field of view; with an approximately 300-mm-by-20-mm area and good soft-x-ray efficiency, the tri-segmented HRC-S is the primary read-out for the LETG, providing spectral coverage shortward of 160 Å.

AXAF CCD Imaging Spectrometer (ACIS) The Pennsylvania State University (PSU) and the Massachusetts Institute of Technology (MIT) designed and fabricated the ACIS with Lockheed–Martin. The ACIS-I and ACIS-S employ large-format (25-mm square) CCDs with 24-μm-square (0.5 arcsec) pixels, covered with an aluminized-polyimide optical blocking filter. All I CCDs and 4 of 6 S CCDs are front-side devices, with little response below 0.4 keV; 2 S CCDs are back-side, affording useful response down to 0.2 keV. With a 50-mm-square area, ACIS-I has a 17-arcmin field of view; with a 150-mm-by-25-mm area, the ACIS-S is the primary read-out for the HETG.

Focal-plane Solid-State Detector (SSD_X) One of the 3 detectors of the HRMA X-ray Detector Assembly (HXDA) is a solid-state detector, designated "SSD_X". The SSD_X is identical to the BND (monitor) detector SSD_5 (§1.1.2). Except for the absence of a radioactive calibration source, the SSD_X aperture wheel is also identical to that of SSD_5.

Focal-plane Flow Proportional Counter (FPC_X) Another of the 3 HXDA detectors is a Flow Proportional Counter, designated "FPC_X". The FPC_X is identical to the 5 BND (monitor) FPCs (§1.1.2). A 2-degree-of-freedom aperture plate, with circular apertures up to 35-mm-diameter for measuring encircled energy and slits for measuring dispersed spectra from the OTGs, lies in front of FPC_X.

High-Speed Imager (HSI) The third HXDA detector is the High-Speed Imager, an uncoated microchannel plate (MCP), with 18-mm-diameter active area and 6.4-μm (0.13-arcsec) read-out resolution.

ACIS Two-Chip (ACIS-2C) The ACIS team (PSU and MIT) and SAO designed, fabricated, and operated the ACIS two chip (ACIS-2C), comprised of one front-side and one back-side flight-type CCDs.

1.2 Calibration activities at the XRCF

Occurring in 12 at-vacuum phases (§1.2.1), calibration activities at the XRCF occupied 6 months of intense (around-the-clock) activity over a one-year period. During this period, calibration of AXAF-observatory subsystems occupied 4 months (§1.2.2), including 3 x-ray months of data collection.

1.2.1 Calibration phases

Table 1 shows the purpose, configuration, and duration of the dozen AXAF-related phases during which the XRCF Instrument Chamber was at vacuum and x-ray data were being acquired. XRCF calibration of the (flight) AXAF observatory system or subsystems occurred in 6 vacuum phases, which were required for planned change-out of focal-plane instrumentation and for repairs to ground-support equipment.

Table 1: XRCF configurations for the AXAF calibration.

CMDB	Phase	X-ray optic	Gratings	FP instrument	Days
	HXDS T&V 1	TMA	TOGA	HXDA	7
A	Rehearsal 1	TMA	TOGA	HXDA	12
B	Rehearsal 2	TMA	TOGA	ACIS-2C	7
	HXDS T&V 2	TMA	TOGA	HXDA	10
C	Calibration 1.1	HRMA	LETG, HETG	HXDA	4
D	Calibration 1.2	HRMA	LETG, HETG	HXDA	26
E	Calibration 1.3	HRMA	LETG, HETG	HXDA	14
F	Calibration 2.1	HRMA	LETG, HETG	ACIS-2C	16
G	Calibration 2.2	HRMA	LETG, HETG	HRC	24
H	Calibration 2.3	HRMA	LETG, HETG	ACIS	8
I	Cross-calibration 1	none	none	ACIS	10
J	Cross-calibration 2	none	none	HXDA	10

1.2.2 Observatory calibration timeline

During daily meetings led by Project Science, the Science team planned impending measurements in a detailed Calibration Measurements Data Base (CMDB), maintained by the AXAF Science Center (ASC). Based on the CMDB, the TRW Test Conductor prepared a test-list script for conducting the planned measurements.

Table 2 shows all calibration phases during which the flight optic (HRMA) was present — namely, CMDB series C–H (see Table 1). Recorded in Table 2, for each phase, are start date of the first measurement, end date of the last measurement, duration in x-ray days, total integration time, number of measurements, and average efficiency ((integration days)/(x-ray days)). Despite a few failures in ground-support equipment, which were eventually rectified, daily — and, in some cases, real-time — replanning of the CMDB enabled useful data collection to continue, with minimal loss of efficiency.

Table 2: Timeline for AXAF calibration measurements at the XRCF.

CMDB	First x ray	Last x ray	X-ray days	Integ. days	Number	Efficiency
C	12/19/1996	12/24/1996	4.40	0.76	96	0.172
D	12/31/1996	01/26/1997	25.71	8.07	799	0.314
E	01/28/1997	02/11/1997	13.58	6.23	277	0.459
F	02/22/1997	03/10/1997	16.46	8.19	584	0.498
G	03/19/1997	04/12/1997	23.84	16.31	1111	0.684
H	04/17/1997	04/26/1997	8.25	5.50	303	0.666
			92.24	**45.05**	**3170**	**0.488**

1.3 Project Science analyses

Project Science is performing analyses of certain data from the AXAF calibration at the XRCF. The remainder of this document constitutes our preliminary report on these analyses, which we summarize

briefly below.

1.3.1 BND data for XSS monochromators

In view of its necessity for analyzing many calibration measurements performed with the flight instruments, our highest priority is the analysis of BND data for the DCM and HIREFS monochromators (§2). Owing to potentially large spatial variations in the monochromators' beams and to possible higher-order contributions to the spectral content, these data require analyses differing from those for the EIPS, which the Mission Support Team is performing.

1.3.2 SSD internal calibrator

A radioactive source in the SSD_5's aperture wheel permits calibration of the SSD_5's gain and energy resolution and monitors changes in its response, e.g., due to accumulation of ice on the detector's window. Knowledge of changes in the SSD_5's response is critical for those measurements for which SSD_5 was the primary monitoring detector. Thus, our next highest priority is analysis of SSD_5 data taken with its calibration source in place (§3).

1.3.3 SSD continuum measurements

To complement HRMA calibration measurements using the EIPS optimized for line emission and the focal-plane FPC (FPC_X), the HRMA calibration included measurements using the EIPS optimized for continuum emission and the focal-plane SSD (SSD_X). These allow simultaneous measurement of the HRMA effective area for energies exceeding about 1 keV, at the spectral resolution of the SSD. In view of the importance of accurately calibrating the effective area, the analysis of the SSD continuum measurements (§4) is a high priority.

1.3.4 Flight Contamination Monitor (FCM)

The HRMA's Forward Contamination Cover (FCC) contains 16 (1 per shell quadrant) radioactive calibration sources. This system of sources, the Flight Contamination Monitor (FCM), will serve to confirm the ground-to-orbit transfer of the AXAF flux scale, which could be compromised by post-XRCF changes in the contamination of the mirrors' surfaces. Hence, the analysis of the FCM data (§5) provides a baseline for comparison to similar measurements to be acquired during the orbital activation of AXAF.

1.3.5 Limits on HRMA contamination

Having recognized the potential influence of contamination on AXAF performance, the AXAF Project has maintained rigorous contamination controls. While all contamination monitoring indicates that the HRMA should be quite clean, it is important to confirm this in the x-ray calibration measurements. In that this is derivative to other analyses of the calibration measurements, the use of x-ray data to set limits on HRMA contamination is just starting (§6).

2 BND data for XSS monochromators

2.1 Objectives

This section is the preliminary report on analysis of Beam-Normalization Detector (BND) data acquired during AXAF calibration using the XRCF monochromators — the Double-Crystal Monochromator (DCM) and the HIgh-Resolution Erect-Field Spectrometer (HIREFS^{TM}) reflection-grating monochromator. The goal is to provide, for each calibration measurement, background-corrected flux (photons s^{-1} cm^{-2}) at the HRMA node, incident upon each quadrant of the 4 HRMA mirror shells. Knowledge of spatial and spectral content of the incident beam, combined with measurements made with the focal-plane instruments, allows calibration of AXAF. From Pulse-Height Amplitude (PHA) spectra, we extract spectral content by fitting the data with a *jmkmod* model [10] within the XSPEC [11] spectral fitting package. We determine spatial content through analytic fits to Beam Uniformity (BU) measurements made nonsimultaneously, either during calibration or during pre-calibration source characterization.

Both spectral and spatial beam characteristics of the monochromators differ substantially from those of the other sources used during calibration. Consequently, we describe the sources themselves (§ 2.2) and the analysis procedures (§ 2.3). We then present trends in the results of the data analysis (§ 2.4) and describe the data products and their current status (§ 2.5).

At this point, we have fit the *jmkmod* model to most FPC PHA spectra, extracted the model-predicted count rate for each spectral feature, converted to flux at the HRMA node, and inspected and tabulated these results. Exceptions are spectra taken January 21-23 (CMDB D series) and during ACIS cross-calibration (CMDB I series) using the DCM. As yet, we have not analyzed data obtained with the SSD_5 monitor detector.

We have already analyzed spatial information, extracted from beam-uniformity maps, for a subset of the measurements, mainly those with a relatively uniform beam. Soon, we shall complete convolution of the beam uniformity and the spectral content. Later, after FPC efficiencies (§2.2.2) have been calibrated, we shall re-analyze those data requiring a calibrated FPC response.

2.2 Measurement descriptions

The X-ray Source System (XSS, §1.1.1) includes 2 monochromators — the Double-Crystal Monochromator (DCM) and the HIgh-Resolution Erect-Field Spectrometer (HIREFS^{TM}). In that the characteristics of the DCM and HIREFS differ substantially from those of the other XSS sources, we first describe the monochromators' unique features as they pertain to reduction and analysis of XRCF data (§2.2.1). We also describe relevant properties of the BND FPCs (§2.2.2, also §1.1.2) and briefly review characteristics of the raw data (§2.2.3). For more details, see presentations from the 1996 June Calibration Readiness Review, at `http://wwwastro.msfc.nasa.gov/xray/xraycal/xssrr`.

2.2.1 Monochromators

Double-Crystal Monochromator (DCM) Figure 2 is a schematic of the DCM. Turret-1 rotation selects the energy satisfying the Bragg condition; Turret-2 rotation then makes the 2 crystal faces parallel. Turret-2 translation along the optical axis holds fixed the beam displacement and, hence, the apparent source position. Attached to the DCM is the Rotating-Anode Source RAS7 (also called RAS North), containing a tungsten anode. The AXAF calibration measurements used only 3 of the 5 turret faces — Thallium Acid Phthalate (TAP001) for 0.7–2.3 keV, germanium (Ge111) for 2.1–8.5 keV, and abraded silicon (aSi400) for 6–12 keV.

Most calibration measurements using the DCM employed a "mini-scan" while setting the energy, in order to optimize the flux. During a DCM mini-scan, typically lasting about 30 s, FPC_5 monitored the flux while Turret 2 rotated in small steps. For some mini-scans, FPC_5 was in its home position rather than at the Facility Optical Axis (FOA), which often resulted in a less uniform beam over the HRMA.

Although the RAS7 operates at high voltage to generate a strong continuum, the tungsten (W) anode also produces several W lines with large equivalent widths, the most prominent being M$\alpha_{1,2}$ (1.775 keV), Mβ (1.835 keV), and Mζ_1 (1.384 keV). The DCM's beam is slightly energy dependent in its dispersive direction, aligned to the XRCF Y (horizontal) axis. This results in significant beam nonuniformity when

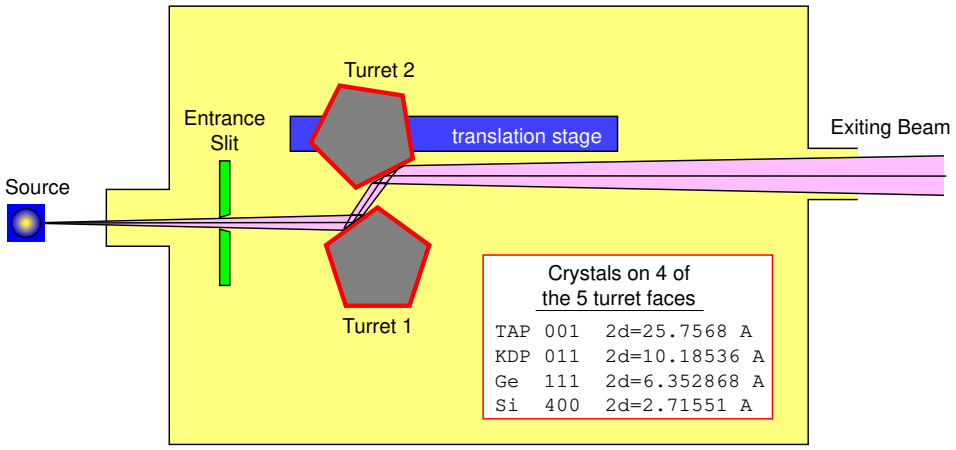

Figure 2: Schematic top view of the optical elements and path for the DCM-RAS7 monochromator. X rays from RAS7 Bragg reflect off the parallel crystal faces of the pentagonal turrets. The calibration of AXAF employed only the TAP, Ge, and Si crystals.

the DCM is tuned to energies near these spectral lines, the strongest of which lie in the TAP energy range. Furthermore, measurements made using the TAP crystal showed additional beam nonuniformity and nonreproducibility, possibly due to waviness of the crystal's surface. In contrast, the Ge beam proved to be highly uniform: The only W lines within the Ge operating energy range are $L\alpha_1$ (8.398 keV) and $L\alpha_2$ (8.335 keV), at the extreme end of its range; furthermore, the crystal's surface is quite flat.

While the contribution of higher spectral orders is generally small for the DCM, we included them as separate lines in fitting the FPC PHA spectra. Higher orders are most prominent in the energy range 1.5–2.2 keV for the TAP crystal. For the Ge crystal, higher spectral orders are very weak.

High-Resolution Erect-Field Spectrometer (HIREFS) Figure 3 is a schematic of the HIREFS^{TM} monochromator, which offers 4 selectable reflection gratings. The AXAF calibration measurements used only 3 of the 4 gratings — SX for 0.8–1.9 keV, SA for 0.25–1.2 keV, and, rarely, SB for 0.1–0.4 keV. The HIREFS's beam is nonuniform, both in its dispersive direction (XRCF Y, horizontal) and in its cross-dispersive direction (XRCF Z, vertical), typically varying by ±20% over the HRMA's aperture.

Attached to the HIREFS is the Rotating-Anode Source RAS14 (also called RAS South), containing a tungsten anode. Owing to scattering in the HIREFS, the strongest W line in the HIREFS energy range, M$\alpha_{1,2}$ at 1.775 keV, appears in all FPC PHA spectra of moderate photon counting rate, for which the FPC gain permitted detection of this line. In addition, higher spectral orders are often strong, particularly at low energy ($E \lesssim 0.6$ keV) for the SA grating and throughout the SB energy range, but are absent for the SX grating due to a 2-keV cut-off in the HIREFS optics. Consequently, the spectral fitting algorithms (described below) include higher-order lines and the scattered M$\alpha_{1,2}$ line, in addition to the monochromator's first-order line.

2.2.2 Flow Proportional Counters (FPCs)

The 5 FPCs used as Beam Normalization Detectors [12] are FPC_5, FPC_HT, FPC_HB, FPC_HS, FPC_HN, corresponding to the FPC in Building 500 and the 4 BND–HRMA (BNDH) detectors located above, below, south, and north of the HRMA entrance aperture (§1.1.2). *For this preliminary report, we assume that all 5 FPCs are identical.* Figure 4 shows the adopted quantum efficiency for the FPCs.

For monochromator energy settings above about 0.4 keV, the moderate spectral resolution of an FPC is sufficient to separate the spectral orders. However, below ∼ 0.4 keV (HIREFS SB and SA gratings), multiple orders overlap so much that the XSPEC fitting engine cannot reliably distinguish individual orders. Similar difficulties arise, again with the HIREFS, when orders overlap with the scattered W-M$\alpha_{1,2}$ line at 1.775 keV. For either monochromator, the continuum flux is negligible. Besides the x-ray

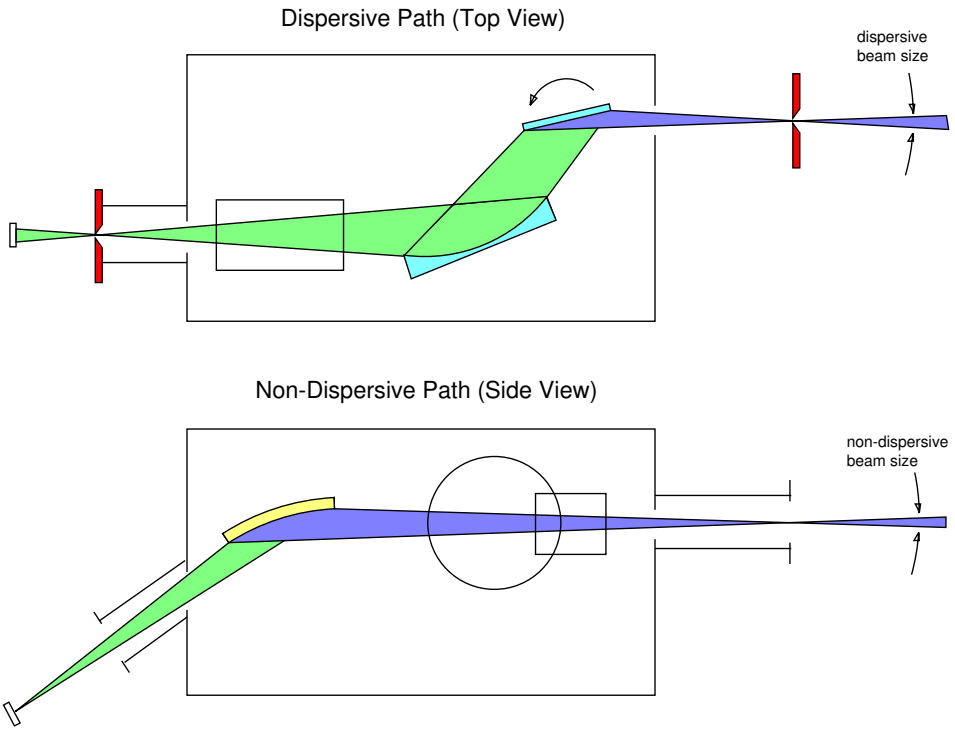

Figure 3: Schematic of the optical elements and path for the HIREFS-RAS14 monochromator. X rays from RAS14 reflect off a flexible astigma-adjusting mirror, then a spherical mirror, before being dispersed by a selectable reflection grating and focussed (in the dispersive direction) onto the exit slit.

lines themselves, the FPC's argon/methane gas mixture (P10) effects an escape peak, ~ 2.95 keV below each spectral 'line'. In the spectral analysis, then, we model each escape peak as a separate line, at known energy, and add the rates of the line and its corresponding escape peak.

For purposes of spectral fitting with model *jmkmod* (see below and [10]), we assume the following detector characteristics (B. Wargelin, e-mail 1996 Feb 26): 200-Å Al over a 1.065-μm polyimide film window; 0.9025 mesh geometric transmission, and 5.36-cm active depth. FPC_5 has an aperture slide with 36, 12, 4, and 1 mm diameter circular apertures. All 4 FPC_H detectors have an open aperture area of 35.75 cm^2; FPC_HN also has an insertable 36-mm-diameter aperture door, used primarily for mapping. Currently, we use the detector software estimate of the dead time, which is included in the PHA spectral data files.

2.2.3 Raw data

We obtained the raw data used in the analysis from the Mission Support Team (MST) mirror site. The MST document "XRCF Phase 1 Testing: Preliminary Results", Chapter 16, discusses the locations and formats of the raw data. Raw data include separate PHA files for each detector, for each measurement, and for each iteration; and they include sum files for each detector and each measurement. Here, an iteration denotes an exposure of fixed duration, short relative to the total measurement time. Typically, individual exposures ranged from 20 s to 90 s, depending upon measurement type and the focal-plane instrument. In addition to these data, the analysis requires ancillary data, such as the MST archived source parameter logs (`xsslog`), detector aperture logs (`aperlog`), and detector stage positions (`stglog`), all of which are on the mirror site. Using the IRIG time stamps included in each data and log file, we then correlate all data for each measurement.

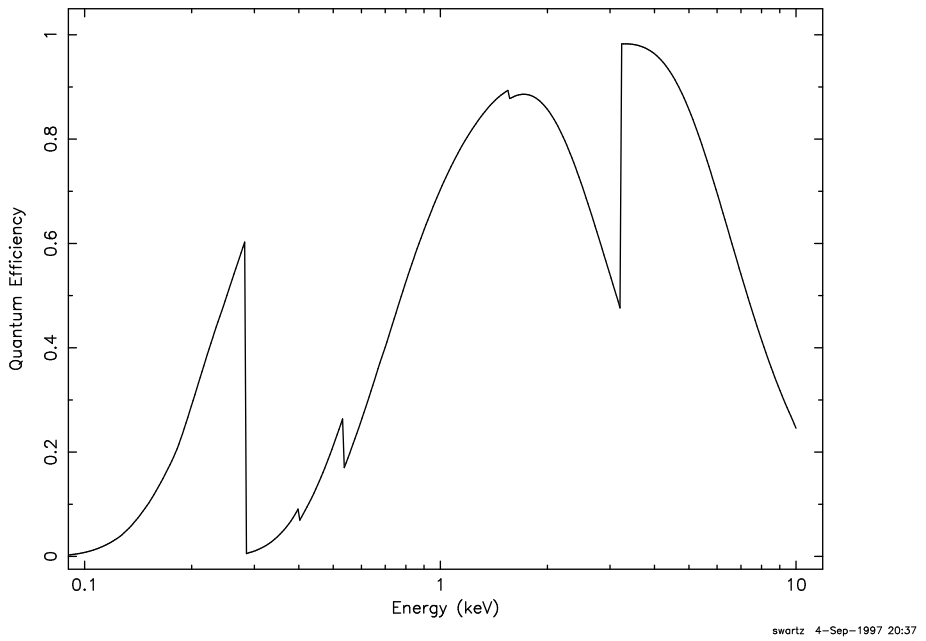

Figure 4: Quantum efficiency curve adopted for analysis of the Flow Proportional Counter (FPC) data.

2.3 Data analysis procedures

In the reduction and analysis of the data, the major stages, in chronological order, are these:

1. Identify and accumulate raw and ancillary data and condense these to a manageable state for each (monochromator) measurement (§2.3.1).

2. Determine the spectral content of these data using model *jmkmod* within the XSPEC spectral-analysis package (§2.3.2).

3. Separately determine the spatial content through fitting beam-uniformity measurements ('maps') to physically reasonable analytic functions using *Mathematica*^{TM} (§2.3.3).

4. Convolve results of (3) with (2) to define the flux incident on individual HRMA quadrants (§2.3.4).

2.3.1 Data acquisition and preprocessing

Certain header fields within the sum file contain HXDS run identification (`runid`) and information from the CMDB which helps identify the measurement — source (`srcType`), measurement type (`measureType`), and CMDB identification `trwid`. However, many beam-uniformity measurements occurred during 'breaks' in the XRCF calibration and are not in the CMDB. Although each of these has a RUNID, it has no TRWID and thus is not readily identified. Tables 3 and 4 list the RUNIDs of DCM and HIREFS, respectively, beam-uniformity maps obtained outside the CMDB.

We process data from the MST mirror site as follows:

1. Identify monochromator measurements by searching (parsing) detector 'sumfiles'.

2. Accumulate a list of RUNIDs, TRWIDs, and dates data were taken. The date identifies the data-file and log-file locations on the mirror site.

3. Correlate PHA data files to monochromator energy settings, using xsslog files and IRIG time stamps.

Table 3: DCM beam-uniformity maps outside CMDB

RUNID	Date	Grating	Energy	RUNID	Date	Grating	Energy
111952	970213	Ge	3.750	113400	970317	Ge	2.560
111953	970213	Ge	3.750	113401	970317	Ge	2.190
111960	970213	Ge	6.000	113403	970317	Ge	2.260
111961	970213	Ge	6.000	113405	970317	Ge	2.350
111974	970213	Ge	7.800	113407	970317	Ge	3.500
111975	970213	Ge	7.800	113415	970317	Ge	4.510
111978	970213	Ge	7.800	113417	970317	Ge	4.900
111979	970213	Ge	7.800	113419	970317	Ge	5.060
111984	970213	TAP	1.200	113435	970317	Ge	2.560
111990	970213	TAP	1.550	113444	970317	Ge	5.250
111997	970213	TAP	2.100	113446	970317	Ge	5.650
113386	970316	TAP	1.530	113448	970317	Ge	6.300
113387	970316	TAP	1.570	113450	970317	Ge	9.000
113388	970316	TAP	1.400	113457	970317	Ge	2.560
113389	970316	TAP	1.950	113459	970317	Ge	2.190
113391	970316	TAP	2.050	113463	970318	TAP	1.570
113392	970316	TAP	2.100	113471	970318	TAP	1.570
113393	970316	TAP	1.700	113473	970318	TAP	1.900
113394	970316	TAP	1.900	113475	970318	TAP	1.950
113395	970316	TAP	1.980	113477	970318	TAP	1.980
113396	970316	TAP	1.800	113480	970318	TAP	2.050
113398	970316	Ge	2.230	113482	970318	TAP	2.100
113399	970317	Ge	2.290				

4. Link the data files on the mirror site to a pre-defined local disk area.

5. Create a bi-spectrogram from the PHA data files — pulse-height channel *vs.* iteration number — in QDP-readable (ASCII) format and in FITS image format.

6. Co-add data in appropriate PHA data files to create a single PHA file for each detector, measurement, and energy, omitting data obtained during monochromator translations or mini-scans. The monochromator control computer records the IRIG time whenever a new energy is requested through software. To avoid periods of monochromator translations and mini-scans, we ignore PHA data taken during ± 35 seconds of this time. Visual inspection of the bi-spectrograms confirms that the undesired data have been filtered. The resulting PHA files have the same format as the original ones, the `liveTime` being the accumulated time for the sequence of original files.

7. Create XSPEC-readable FITS files from the new (co-added) PHA files, using the MST script `pha2xspec-fits`.

Table 4: HIREFS beam-uniformity maps outside CMDB

RUNID	Date	Grating	Energy	RUNID	Date	Grating	Energy
113282	970312	SA	0.523	113336	970314	SX	1.569
113285	970312	SA	0.539	113338	970314	SX	1.569
113292	970313	SA	0.625	113340	970314	SX	1.617
113294	970313	SA	0.640	113341	970314	SX	1.617
113296	970313	SA	0.785	113344	970314	SX	1.962
113311	970313	SA	1.046	113346	970314	SX	1.250
113313	970313	SA	1.078	113348	970314	SX	1.280
113315	970313	SA	1.177	113350	970314	SX	1.876
113319	970313	SA	0.625	113352	970314	SX	1.919
113320	970313	SA	0.640	113354	970314	SX	1.546
113321	970313	SA	0.785	113357	970315	SX	1.384
113322	970314	SA	0.523	113359	970315	SX	1.775
113323	970314	SA	0.539				

xsslogs For the DCM, the relevant xsslogs fields are `DCM.date` and `XB6HDCT1RT`, the execution time of the DCM energy-setting command and the resulting Turret-1 position in motor steps, respectively. Equation 1 gives the fitting function for the crystal grazing angle θ (radians), in terms of the Turret-1 position s (motor steps):

$$\theta(s) = (\frac{\pi}{180^\circ})[0.3333^\circ - \frac{(s - s_i)}{r_i}] \ , \tag{1}$$

with s_i (steps) the Turret-1 offset and r_i (steps/°) its conversion factor, for crystal i. Then, for crystal grazing angle θ (Eq. 1), Equation 2 gives the corresponding Bragg energy:

$$E(\theta) = \frac{(12.3984 \text{ keV Å})}{2d_i \sin\theta} \ , \tag{2}$$

with d_i the lattice spacing of crystal i. Table 5 lists the fitting parameters t_i and s_i and the lattice spacing d_i, for each crystal employed in the calibration.

Table 5: DCM parameters

Crystal plane	Lattice d_i (Å)	Offset s_i (steps)	Conversion r_i (steps/°)
TAP 001	12.8784	7820115.0	25538.819
Ge 111	3.266434	4160079.0	25386.677
aSi 400	1.357755	2331545.0	25384.629

For the HIREFS, the relevant xsslogs fields are `HIREFS.date` and `XB6HHRWLEN`, the execution time of the HIREFS energy-setting command and the resulting HIREFS wavelength (in Å), respectively.

Backgrounds The TRWID measurement type BG identifies background measurements. During ACIS set-up (measurement type SG), additional background measurements occurred. Typically, each background measurement comprises several iterations. For analysis purposes, we first plotted these to check

for anomalies, and then co-added channel-by-channel, and wrote the data as XSPEC-readable FITS files. The PHA file header (in field `voltage_V`) documents the detector high-voltage setting, which we tabulated along with the data acquisition time, to facilitate matching backgrounds to measurements.

2.3.2 Spectral content

The spectral data reduction fits the model *jmkmod* [13] to the PHA data, within the XSPEC [11] spectral fitting package. The analysis follows closely that elucidated in reference [14] and proceeds as follows:

- Generate XSPEC command files for fitting the co-added PHA files. These command files profit from the fact that the principal spectral features are 'lines' that occur at known energies, corresponding to the selected monochromator setting and multiples thereof. For 'lines' at energies greater than the argon K-shell ionization (3.2 keV), the model also includes the corresponding escape lines. In addition, for HIREFS measurements, the model includes the W-M$\alpha_{1,2}$ line (1.775 keV) generated in the RAS anode and scattered within the HIREFS. The command files also identify a corresponding background, which we subtract using the 'back' command within XSPEC. Because the data show negligible continuum, the model includes no continuum component.

- Fit *jmkmod* in XSPEC to spectra with line energies fixed. Free parameters are gain (relating line energy to channel number), Polyah factor (line width, described in reference [15], shelf-norm parameter (for the partial-charge-collection shelf in channels below each 'line'), line strengths (relative norms), and overall model norm. We set the Fano factor to 0.2, turn off *jmkmod* continuum parameters, and use no additional XSPEC model component.

- Archive details of the fit (XSPEC log file) and a qdp-formatted figure, displaying data and model fit in one panel and the fit residuals in a second panel, as generated for each PHA file analyzed.

- Convert counts/s (from XSPEC fit with XSPEC-generated errors) to photons/s/cm^2 at the HRMA node using aperture areas from aperlogs, quantum efficiencies described previously, and distances from source to detectors and HRMA.

- Place resulting flux (with errors) for all fitted spectral features, along with line energies, identifying parameters (RUNID, TRWID, IRIG times, background TRWID), model free parameters (with errors), fit statistics, Region Of Interest (ROI) used in fit (typically channels 21 to 399), integration times, y and z stage positions, aperture areas, etc., into rdb-format table files (see § 2.5).

For beam-uniformity measurements, the procedure differs slightly:

- Do not co-add PHA spectra for all measurements made at a single energy, because the detector is mapping the beam for a fixed source setting.

- Do not create bi-spectrograms because flux at the mapping detector's position is changing.

2.3.3 Spatial Content

After determining and tabulating (rdb format, § 2.3.2) the spectral content for the beam-uniformity measurements, proceed as follows:

- Fit beam models to the spatial data using the standard packages *Statistics`LinearRegression`* and *Statistics`NonlinearFit`* in *Mathematica*$^{\text{TM}}$.

- Employ two basic functions for fitting to the spatial data:

$$f_1(y,z) = a + bz + cy + dy^2 \tag{3}$$

$$f_2(y,z) = (a + bz)(m + ce^{-(y-y_{\text{line}})^2/2\sigma^2}) \tag{4}$$

- Because the mapping BND has a circular aperture, integrate functions over circular aperture of radius r_0 centered at $\{y_0, z_0\}$.

- Fit polynomial functions (Eq. 3) to data by minimizing Pearson's χ^2 with respect to the model parameters. The *Mathematica* package *Statistics`LinearRegression`* supplies standard errors for the best-fit parameters. Carry out fits for 6 cases of increasing complexity:

  1. Constant: $a \neq 0$ and $b = c = d = 0$.
  2. Linear in z: $a \neq 0, b \neq 0$ and $c = d = 0$.
  3. Linear in y: $a \neq 0, c \neq 0$ and $b = d = 0$.
  4. Quadratic in y: $a \neq 0, c \neq 0, d \neq 0$ and $b = 0$.
  5. Linear in z, linear in y: $a \neq 0, b \neq 0, c \neq 0$ and $d = 0$.
  6. Linear in z, quadratic in y: $a \neq 0, b \neq 0, c \neq 0, d \neq 0$.

  Record values of χ^2, probability of exceeding this value, and probability of the F-ratio relative to the fit to a constant (item 1 above).

- For inadequate fits to the polynomial functions (Eq. 3), perform nonlinear fits to the second function (Eq. 4), which includes a gaussian, using the *Mathematica* package *Statistics`NonlinearFit`*. Carry out fits for 3 cases of increasing complexity:

  1. Gaussian in y: $c \neq 0$ and $a = 1, b = 0, m = 0$.
  2. Constant plus gaussian in y: $a \neq 0, c \neq 0$ and $b = 0, m = 1$.
  3. Linear in z, constant plus gaussian in y: $a \neq 0, b \neq 0, c \neq 0$ and $m = 1$.

  Again, record values of χ^2, probability of exceeding this value, and probability of the F-ratio relative to the fit to a constant.

- Select the function and parameters giving the best fit, evaluate it at the positions of the 4 BND_H detectors, and integrate it over each HRMA shell quadrant. *Note that the best fit is not necessarily a good fit!*

- Place relevant information from previous steps into rdb-format table files, for all significant spectral orders:

  1. Best-fit parameters and their standard errors.
  2. Goodness-of-fit information, such as the value of χ^2, probability of exceeding that value, F-ratio comparison to fit to a constant, root-mean-square residual, etc.
  3. Best-fit function values at the BND_H positions.
  4. Values for the integral of the best-fit function over each HRMA shell quadrant.
  5. Identifiers such as RUNID, TRWID, IRIG time, etc.
  6. Source information such as `srcName` (DCM or HIREFS), `srcType` (TAP, Ge, or aSi for DCM; SB, SA, or SX for HIREFS), source energy, etc.
  7. Any other relevant information, such as aperture area, etc.

- Make *Mathematica* notebooks used in this analysis available on request. These notebooks are ASCII files, portable to any platform, and require *Mathematica* version 3.0 or higher.

2.3.4 Convolution of spectral and spatial information

As the final step, we combine the spectral content for each measurement with the spatial information from the beam-uniformity maps. In this preliminary report, we assume that all 5 FPCs are identical. Thus, we simply scale the flux at the 4 HRMA BNDs, using the beam-uniformity fitting function, to the observed fluxes for a given measurement, as determined from analysis of the 4 BND_H PHA spectra:

- Identify an appropriate BU map for each measurement, based upon information from the spatial and spectral analyses (rdb tables) described above. The spatial properties depend upon monochromator, energy setting, grating or crystal, and, (for the DCM) Turret-2 position. Thus, a suitable pairing matches these 3 (4) source properties.
- Scale the BU fitting function evaluated at the 4 BND_H positions to the fluxes observed in these 4 detectors during the measurement. We use a linear regression, weighting all 4 detectors equally.
- Build a final rdb table similar to the tables built from the spectral fitting results. Instead of a (separate) table for each detector giving flux at the HRMA, the flux is at the HRMA quadrant positions and *independent of detector*.

For multiple energy scans, we follow this same procedure if there was a BU measurement for each energy setting in the scan. For measurements for which an appropriate map is not available, we shall interpolate between BU measurements made at neighboring energies: We have not yet attempted this.

2.4 Results

We identified 30126 DCM and 9106 HIREFS iterations, corresponding, respectively, to 548 and 495 independent RUNIDs. From these, we obtained 952 DCM and 970 HIREFS co-added spectra (independent source energy settings) for each of the 5 FPC BNDs. Thus far, we have determined the spectral content for all HIREFS measurements and 489 DCM measurements; we have not yet processed CMDB D-series or I-series (ACIS flat-field) measurements.

We found 97 DCM and 28 HIREFS beam-uniformity measurements, of which 73 DCM and 2 HIREFS occurred within the CMDB. All monochromator beam-uniformity measurements were performed with the FPC_5 mapper, except 4 unanalyzed DCM measurements with the BNDm̃apper. Thus far, we have analyzed PHA spectra for 73 DCM and 28 HIREFS maps; we have determined spatial content for many of the DCM maps. Due to the volume of data and the inherent lack of an end-user product, such as effective area, we present only a few results here. Hopefully, these will encourage others to utilize these data in determining, e.g., effective areas.

Figure 5 displays 4 XSPEC fit results, representative of the diverse spectral content of the monochromator data. Figure 6 is a representative bi-spectrogram, generated in initial processing of the PHA data. Figure 7 shows examples of beam-uniformity variation with (DCM) energy and crystal.

Figures 8 and 9, respectively, show the maximum flux variation over the beam against monochromator energy. This illustrates the nonuniformity in the TAP beam near 2 keV and the uniformity in the Ge beam. The HIREFS exhibits an inherently nonuniform beam, but on a more manageable scale.

We generated Figures 10 through 12 directly from the rdb tables containing the results of the spectral analysis (§ 2.3.2) of the FPC_HT data. Figures 10 and 11 show the XSPEC-generated error for the first and second order spectral-line flux, for the DCM and HIREFS data, respectively.

For most DCM measurements, the first-order error is typically a couple percent. The range in errors in this order results from the range of fluence in the measurements. The second-order error above ~ 2 keV is unimportant because there is little second-order flux at these energies. Below ~ 2 keV, second (and third) order are small but often detectable (cf. lower left panel, Figure 5).

The first-order error for the HIREFS is typically a few percent. At the lowest energies, where order confusion dominates, and near the W-M lines, the error can be considerably larger. This latter trend occurs for the second-order flux for an energy setting near 0.9 keV (one-half the W-Mα energy). Only a subset of measurements are so affected, because we did not include the scattered W-Mα line in the model for all measurements. Figure 12 shows the model flux and fractional error in the scattered W-Mα line. For the reasons just mentioned, the fractional error in this feature is greatest near 0.9 and 1.8 keV. On the other hand, the W-Mα flux appears relatively independent of the HIREFS energy setting. Thus, we shall re-analyze these data, determining the W-Mα flux from spectra not affected by this 'line confusion' and then freezing the model norm for this line when fitting remaining spectra.

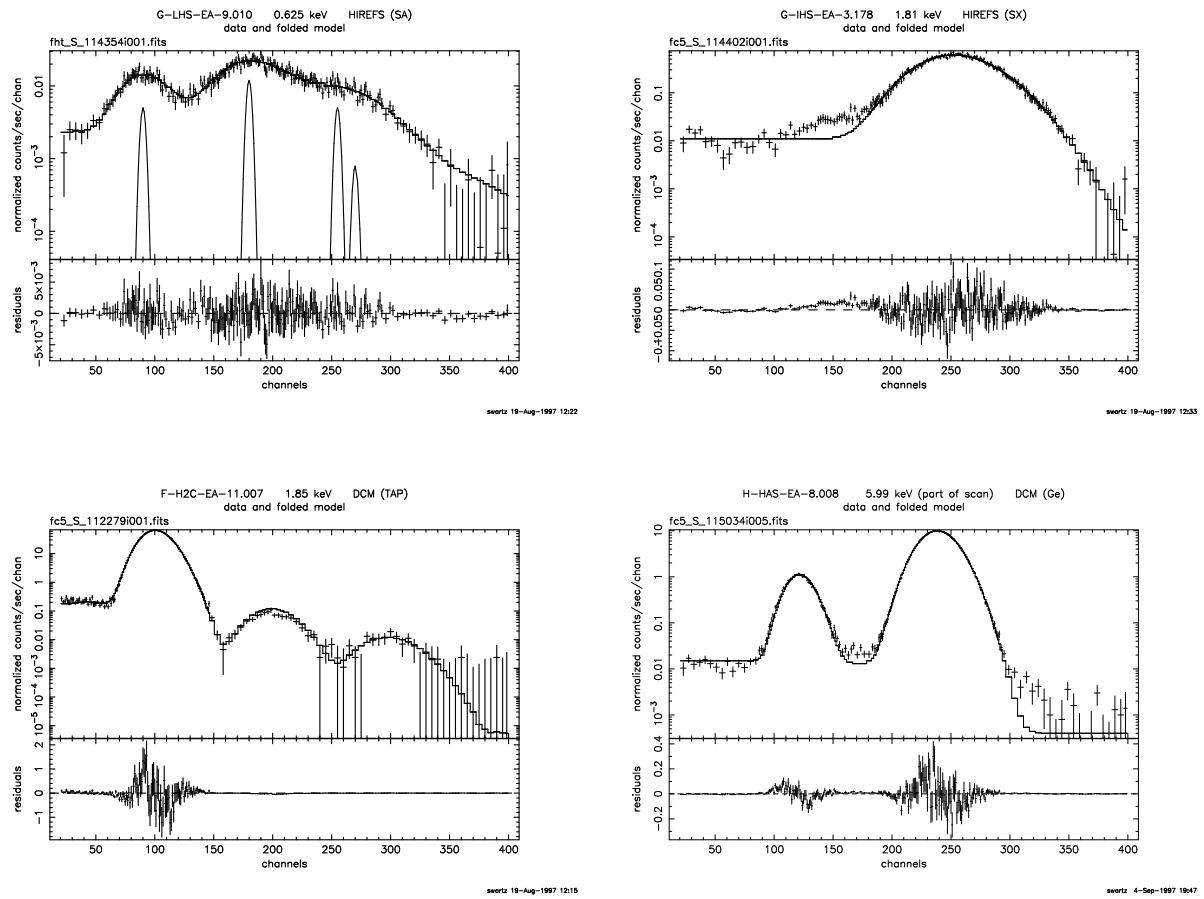

Figure 5: Representative monochromator data and model fits, obtained with the FPCs. Upper left panel shows the confusion among spectral orders that occurs at low energies for the HIREFS SA grating. The auxiliary narrow lines denote, from low to high channel, first and second spectral order, W-Mα scattering, and third spectral order. Upper right panel shows a poor fit to an unidentified shoulder feature. Lower left panel illustrates multiple orders in TAP data; lower right, the Ar escape peak.

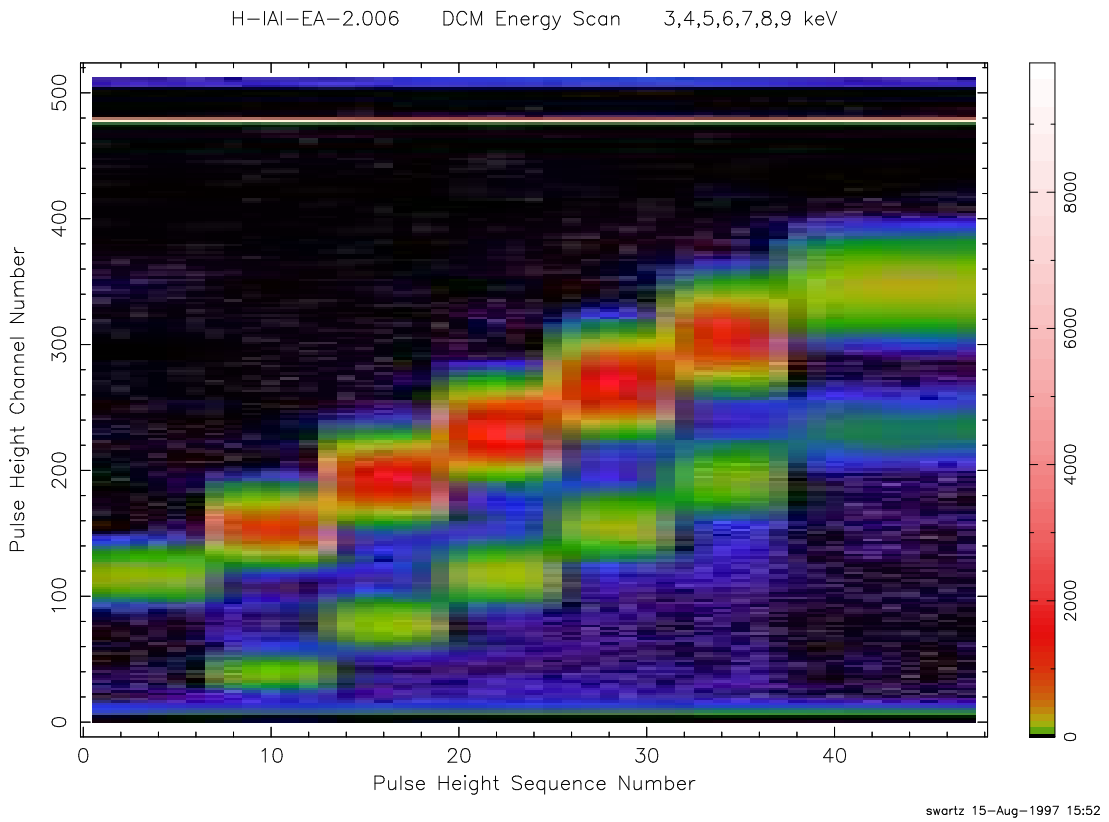

Figure 6: Bi-spectrogram for a DCM energy-scan measurement. Note the escape peak at about 3 keV below the main peak, the changing flux with source energy setting, and the transitions between energy settings during DCM Turrret-2 translations and mini-scans.

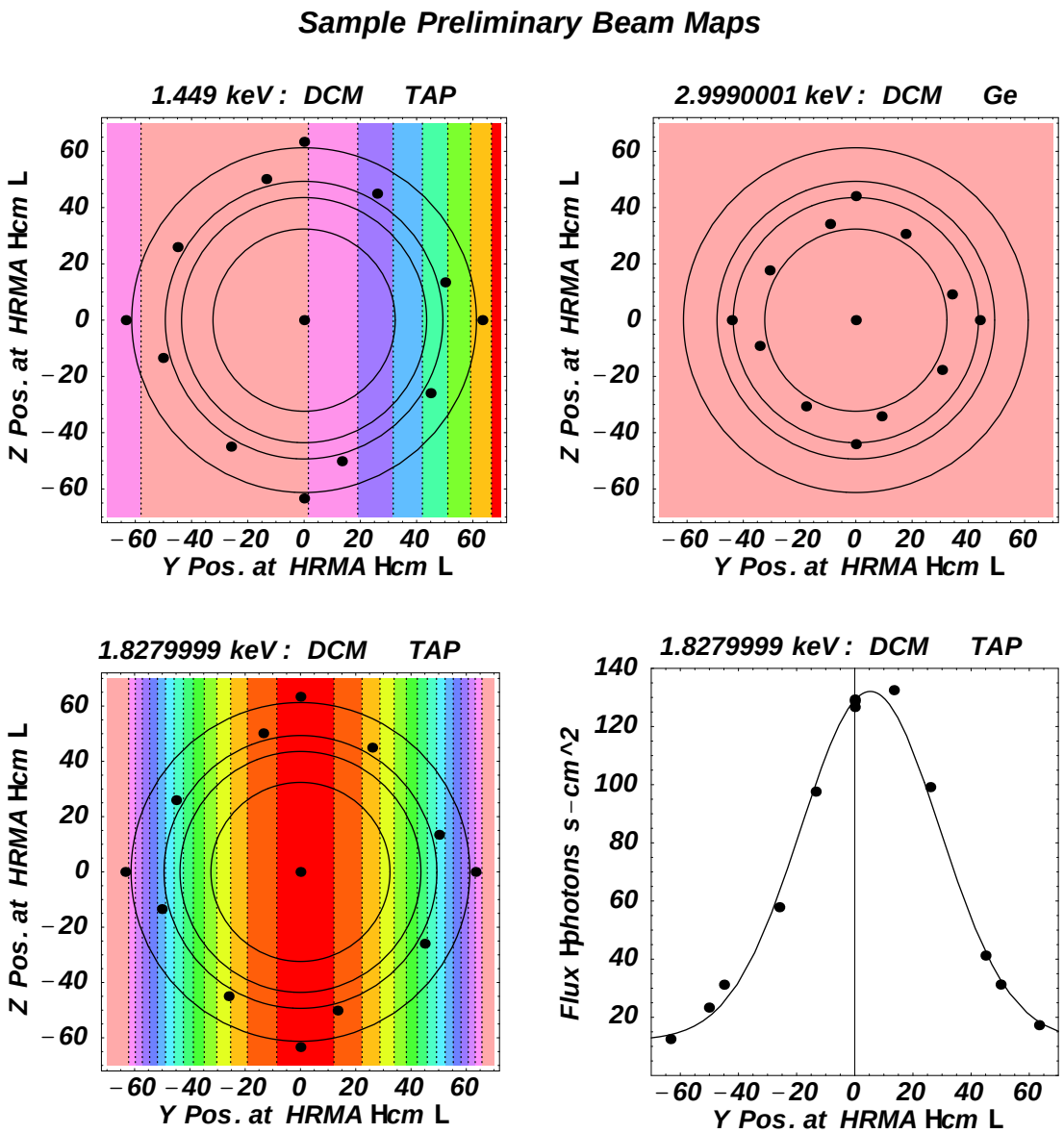

Figure 7: Sample DCM beam-uniformity maps, illustrating relative positions of the 4 HRMA shells (large open circles), positions of mapper detector (small filled circles), and flux contours. Upper panels demonstrate that most of the spatial variation is along the XRCF Y direction. Note that the Ge crystal produces a very uniform beam. Bottom panels show strong nonuniformity near W-Mβ (1.835 keV).

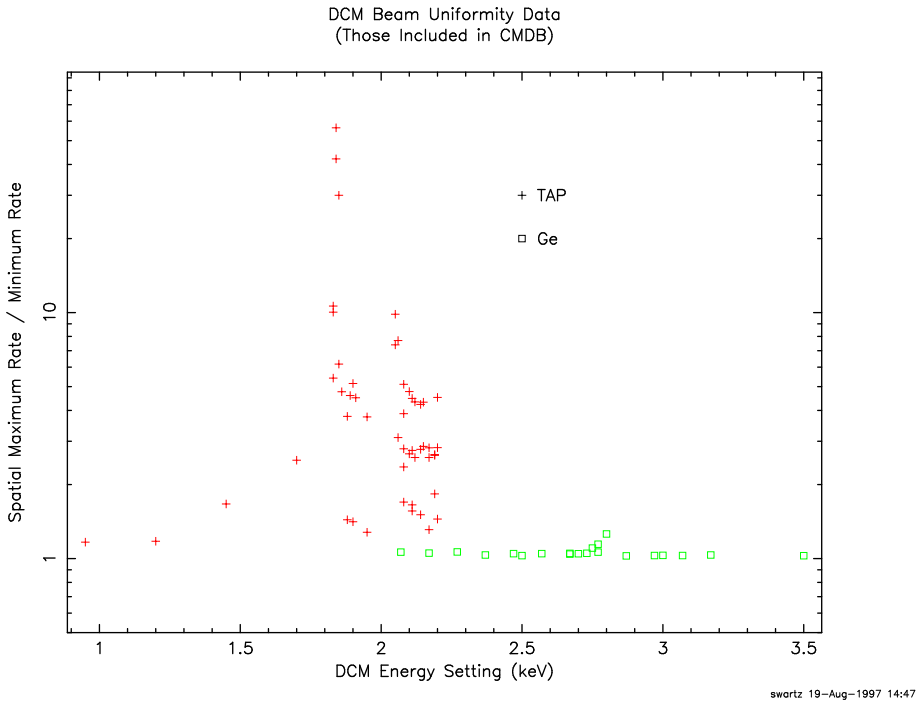

Figure 8: Peak-to-valley spatial variation over regions covered in beam-uniformity maps for the DCM. Note the severe nonuniformity in the TAP beam, particularly near the tungsten-anode M lines, and the relative uniformity of Ge beam. Some of the scatter results from counting statistics.

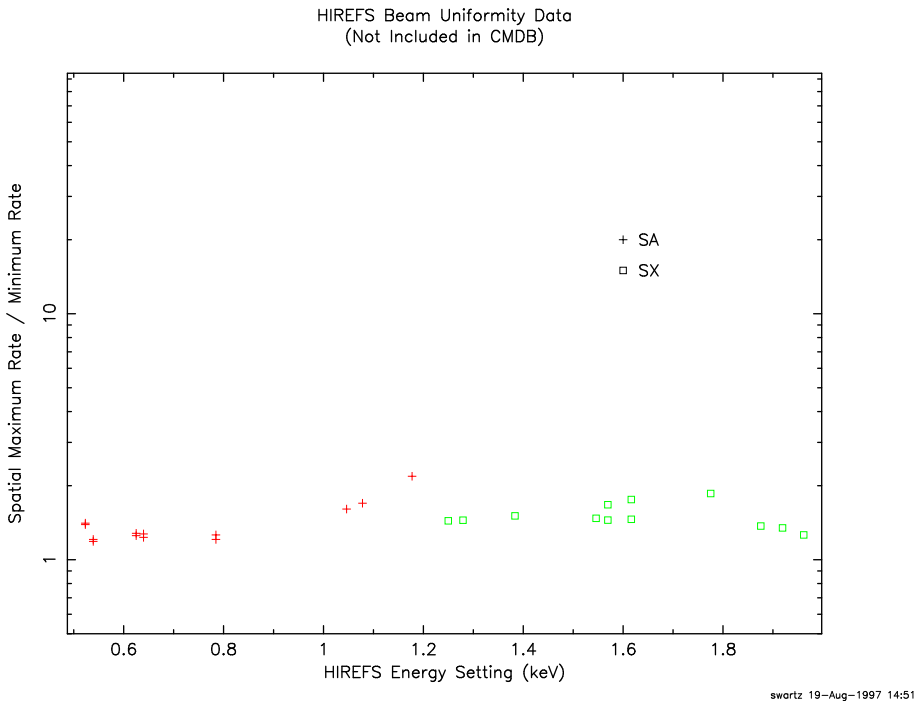

Figure 9: Peak-to-valley spatial variation over regions covered in beam-uniformity maps for the HIREFS monochromator. Note the typical $\pm 20\%$ variation in the HIREFS beam. Some of the scatter results from counting statistics.

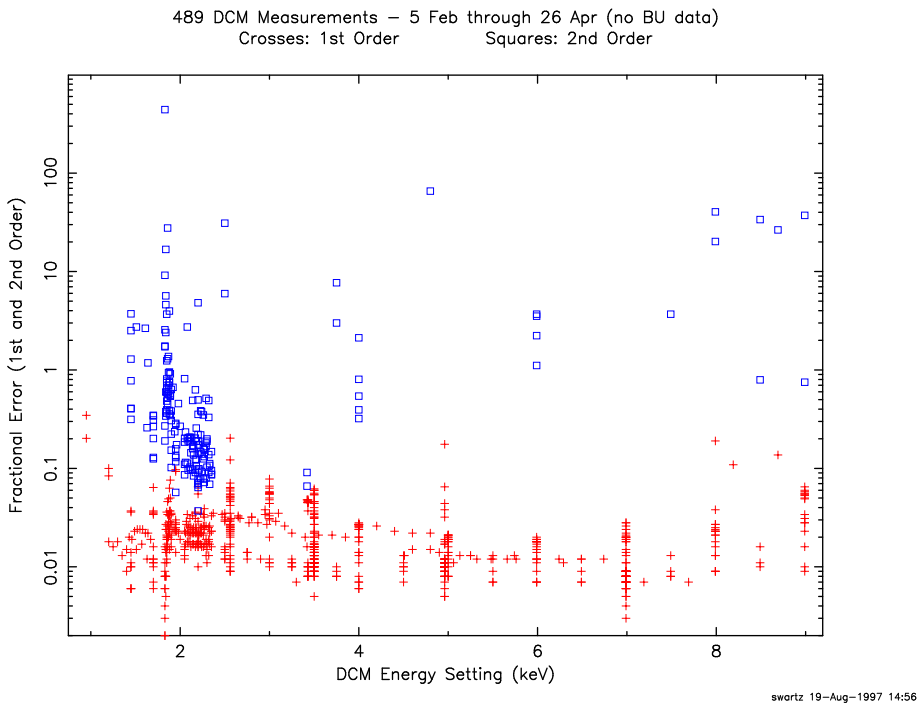

Figure 10: Estimated fractional error in DCM flux for detector FPC_HT.

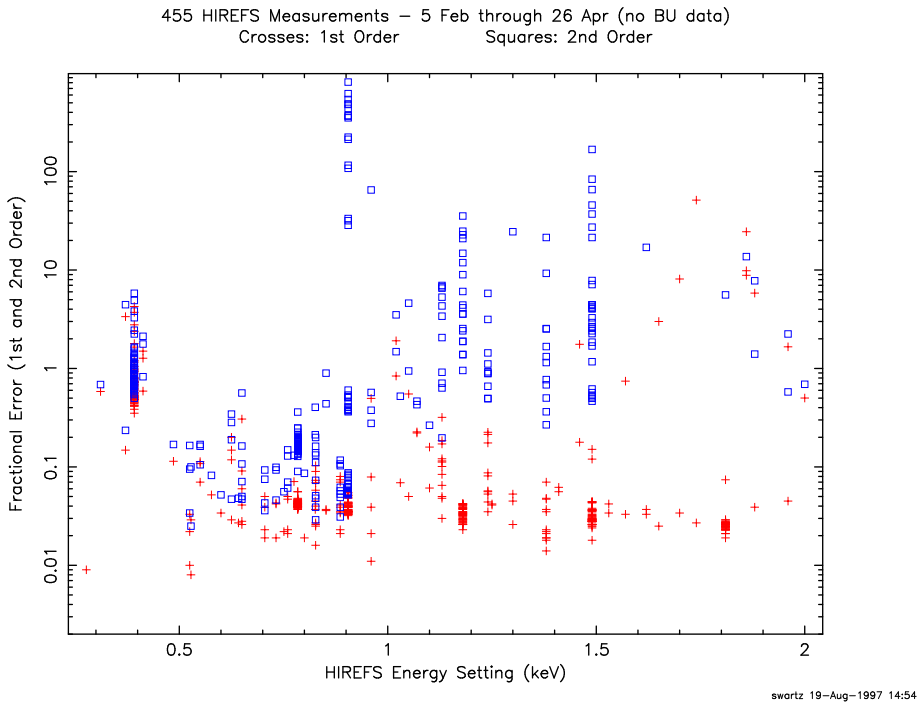

Figure 11: Estimated fractional error in HIREFS flux for detector FPC_HT.

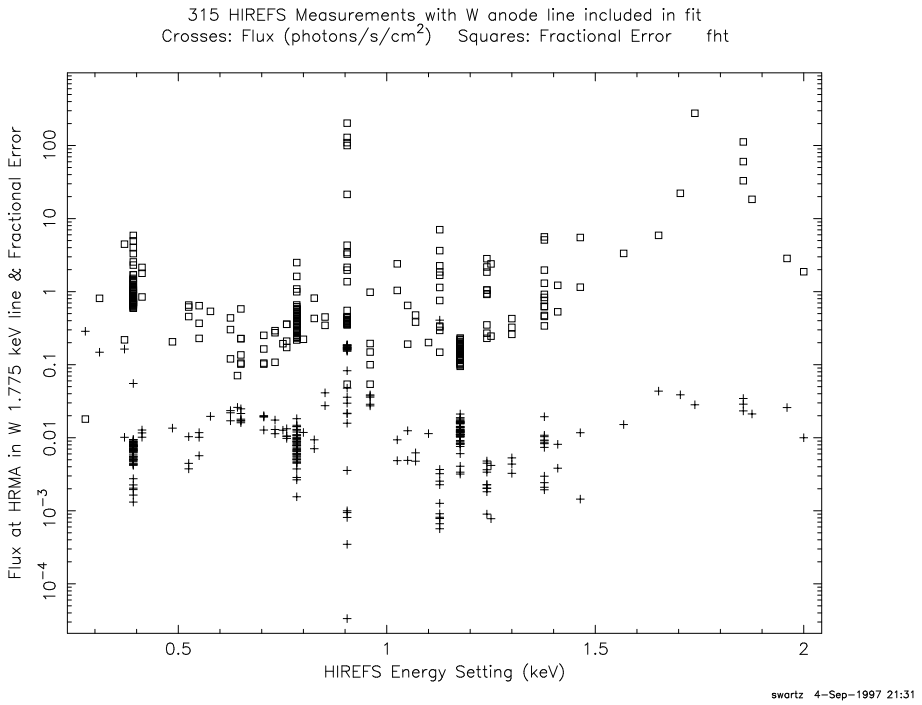

Figure 12: Flux and estimated fractional error in W-Mα line for detector FPC_HT.

2.5 Data Products

2.5.1 Intermediate Products

We have generated several intermediate products for visualizing and understanding the data-analysis process, for estimating limitations and accuracy, and to facilitate reproducing the results:

- Bi-spectrograms (qdp (ASCII), FITS image formats)
- Co-added PHA spectra (rdb, XSPEC-readable FITS) and 'mapping' of raw data to monochromator energy settings (ASCII)
- XSPEC-generated plot files showing spectral data and model fits *vs.* channel number (qdp (ASCII))
- XSPEC-generated 'log' files, containing *jmkmod* fit parameters and their errors, included PHA channels, observed and model count rates over these channels, associated background, and the χ^2 fit statistic (ASCII)
- Beam-uniformity analysis intermediate products, per § 2.3.3.

2.5.2 rdb tables

The primary data product is a set of rdb-formatted tables. For each FPC and for each monochromator combination, we generate an rdb table (10 in all), containing the following information:

- Flux at the HRMA node (photons/s/cm^2), *at the XRCF Y,Z position of the particular BND*, with XSPEC-generated errors, for up to 5 lines (4 spectral orders, plus the W 1.775-keV line for most HIREFS measurements);
- Measurement identifiers (RUNID, TRWID, IRIG time, etc).

Were the beam spatially uniform, these tables would constitute the final product of the analysis.

We have not yet completed modeling the beam-uniformity data. Tentatively, the rdb table for this portion of the analysis will include the following:

- Flux at the HRMA node (photons/s/cm^2), as estimated by the best-fitting analytic function *evaluated at the XRCF Y,Z position of the four BND_H detectors*, with XSPEC-generated errors, for up to 5 lines (4 orders, plus the W 1.775 keV line for most HIREFS measurements);
- Flux at the HRMA node (photons/s/cm^2), as estimated by the best-fitting analytic function *averaged over each of the sixteen HRMA shell quadrants*, with XSPEC-generated errors, for up to 5 lines (4 orders, plus the W 1.775 keV line for most HIREFS measurements);
- Measurement identifiers (RUNID, TRWID, IRIG time, etc);

Tentatively, the rdb table for the final convolution of the spectral and spatial data will include the following:

- Fitted scale factor for normalizing the beam-uniformity predicted flux at the BND_H positions to the flux observed in these 4 BNDs for the measurement;
- Flux at the HRMA node (photons/s/cm^2), *integrated over each of the 16 HRMA shell quadrants*, with errors, for up to 5 lines (4 orders, plus the W 1.775 keV line for most HIREFS measurements);
- Measurement identifiers (RUNID, TRWID, IRIG time, etc) and associated beam-uniformity identifiers (RUNID, TRWID, IRIG time, etc).

In addition, all tables will contain the following ancillary data:

- Monochromator settings (monochromator name, grating or crystal, energy setting, RAS beam current and high voltage);
- Detector settings (detector name, stage position, high-voltage setting, aperture area);
- XSPEC model fit parameters for free parameters, with errors, and fit statistics.

The following is the header section from an rdb table reporting the results of the spectral modeling of the PHA data. The header briefly describes all data contained in its columns and certain additional information useful to the data-product user. We have not yet specified headers for the other rdb data products — beam-uniformity fits and flux incident on HRMA quadrants.

```
# COLUMN DEFINITIONS
#runid:          MST runid
#ymd:            yymmdd date
#trwid:          trwid
#irig:           irigStartTime
#srcName:        source name from sumfile
#srcType:        source anode for EIPS
#srcEnergy:      source energy for monochromator
#detector:       Beam Normalization Detector name
#iter:           iteration number (one per monochromator energy setting)
#BG_trwid:       corresponding background trwid
#eline1:         energy of first line fit (keV)
#flux1:          flux in first line fit (phts/s/cm2) at HRMA nodal point
#flux_err1:      error in flux in first line fit
#eline2:         energy of second line fit (keV)
#flux2:          flux in second line fit (phts/s/cm2) at HRMA nodal point
#flux_err2:      error in flux in second line fit
#eline3:         energy of third line fit (keV)
#flux3:          flux in third line fit (phts/s/cm2) at HRMA nodal point
```

```
#flux_err3:      error in flux in third line fit
#eline4:         energy of fourth line fit (keV)
#flux4:          flux in fourth line fit (phts/s/cm2) at HRMA nodal point
#flux_err4:      error in flux in fourth line fit
#eline5:         energy of fifth line fit (keV)
#flux5:          flux in fifth line fit (phts/s/cm2) at HRMA nodal point
#flux_err5:      error in flux in fifth line fit
#aper_area:      area of aperture in use (cm2)
#stage-y:        detector y-axis stage position (um)
#stage-z:        detector z-axis stage position (um)
#chn_lo:         lower channel included in fit
#chn_hi:         upper channel included in fit
#liveTime:       integration time for this iteration
#obs_rate:       count rate within roi
#obs_rate_err:   uncertainty in count rate within roi
#mod_rate:       model predicted count rate within roi
#Chi_sq:         model chi-squared
#nchan:          number of pha bins included in chi-square calculation
#gain:           model gain parameter value
#gain_err:       model gain parameter value error
#shelfnorm:      model shelf norm parameter value
#shelfnorm_err:  model shelf norm parameter value error
#polyah:         model polyah parameter value
#polyah_err:     model polyah parameter value error
#voltage_V:      detector high voltage setting
# ANCILLARY DATA FILES
#Distances:      http://wwwastro.msfc.nasa.gov/xray/xraycal/distance.htm
#Apertures:      see /pool14/swartz/tables/aper.tab
#FPC_qe:         see /pool14/swartz/tables/fpc.qe
#ssd_qe:         see /pool14/swartz/tables/ssd.qe (data from BESSY)
#mesh_corr:      a mesh correction of 0.9025 is applied to all FPC fluxes
# JMKMOD FIXED PARAMETER VALUES
#fano:          0.20            #bfield:      14500.0
#E_offset:      0.0             #current:         1.0
#ch_off:        0.0             #incline:         0.0
#broad:         0.0             #abswitch:        0.0
#d_gain:        0.0             #phi:           135.4
#contin:        0.0             #theta:          40.2
#E_char:        2.0             #shell:          12.0
#E_width:       0.1             #src1:           35.0
#temper:       15.0             #src2:            6.0
#pressure:    400.0             #src3:            2.0
#argrat:        0.9             #src4:           19.0
#shelfsw:       1.0             #src5:           38.0
#t1norm:        0.0             #src6:           45.0
#t1par:         0.999           #srcthk1:         0.0
#t2norm:        0.0             #srcthk2:         0.0
#t2par:         1.001           #srcthk3:         2.000e-6
#pulser:        0.0             #srcthk4:         1.065e-4
#numcomp:       8.0             #srcthk5:         5.36
#numfil:        6.0             #srcthk6:         0.0
#pileup:        0.0
#pilepar:       1.0
```

3 SSD internal calibrator

3.1 Objectives

This section describes the analysis of spectra taken with the BND Solid-State Detector (SSD_5) when the ^{244}Cm calibration source was in place. The goal is to determine variations of detector parameters (gain and resolution) with time and measure efficiency changes due to accumulation of ice on the detector. The following subsections describe the data and the procedures used to analyze the spectra (§ 3.2) and provide an overview of current results (§ 3.3).

During and preceding calibration of the AXAF observatory, we obtained more than 3500 raw PHA files containing ^{244}Cm spectra. For contemporaneous spectra — i.e., those taken within a few hours of one another — we inspected the light curve for anomalies, excluded those anomalous data, and channelwise added the contemporaneous data to create $\sim$ 120 XSPEC-readable FITS PHA data files. Excluded anomalous data fall into the following categories:

- One measurement used a 2 μsec shaping time; all others used 10 μsec.
- The detector warmed during one measurement, temporarily degrading the energy resolution.
- Spectral lines had a 'shoulder' in some of the early (pre-calibration) data.
- During one iteration, the count rate dropped inexplicably.

3.1.1 Gain and energy scale

The photon energy E is related to the SSD offset, gain G, and channel through

$$E(\mathrm{eV}) = \mathrm{offset} + G \times \mathrm{channel} \ ; \tag{5}$$

the resolution function is

$$\sigma(\mathrm{eV}) = [C + P \times E(\mathrm{eV})]^{1/2} \ . \tag{6}$$

Figures 13 and 14 show the temporal variation in the model's (§ 3.2) gain and offset parameters. Figure 15 displays the resolution parameters, C and P, against time.

3.1.2 Icing

Figures 16, 17, and 18 show temporal variations of several of the more important model (§ 3.2) fitted line strengths.

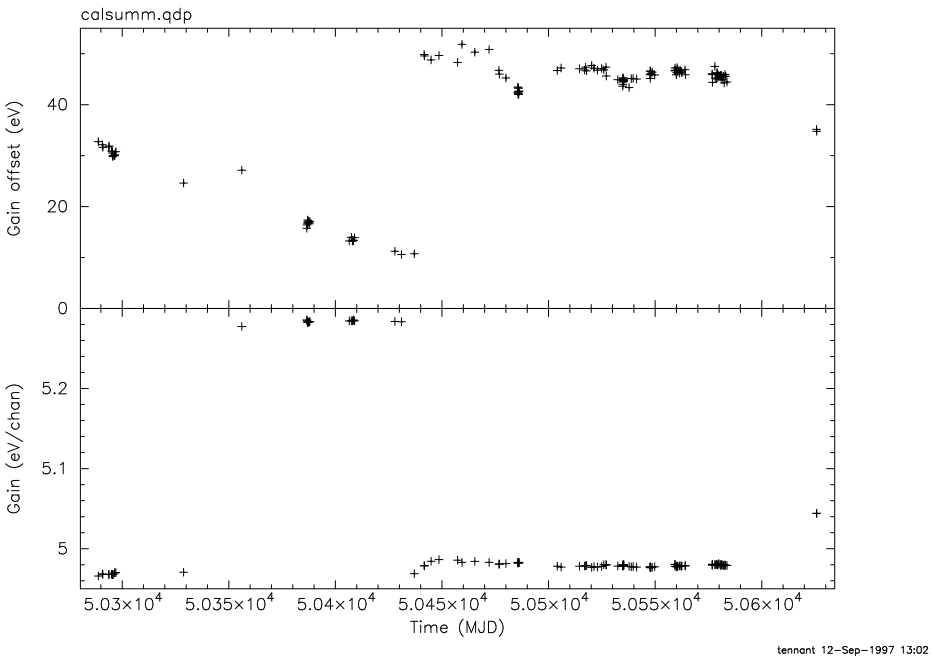

Figure 13: Temporal dependence of model gain and gain offset parameters.

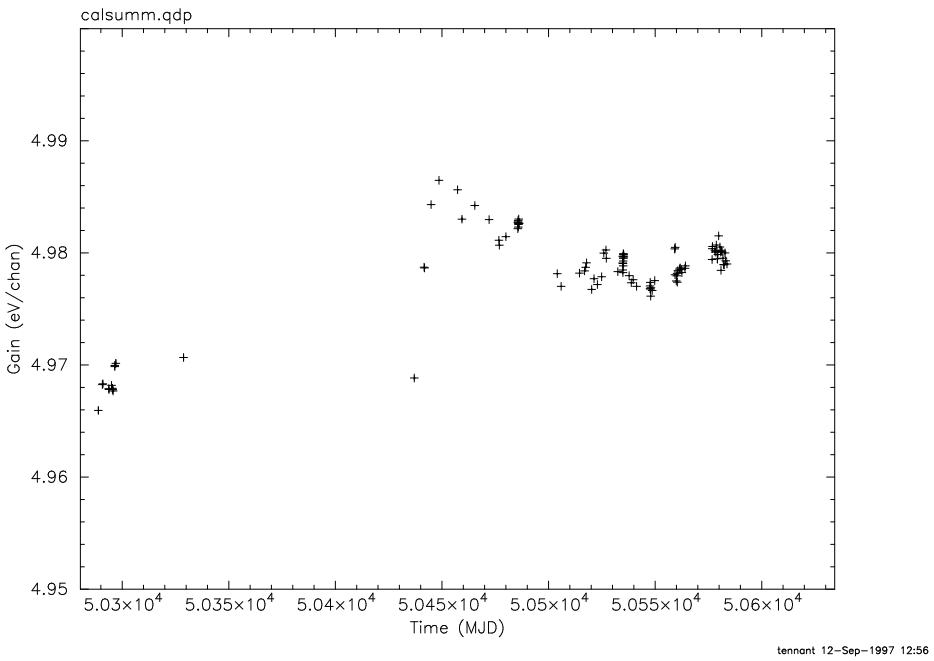

Figure 14: Temporal dependence of model gain parameter excluding high-gain interval from MJD $\sim$ 50350 – 50430.

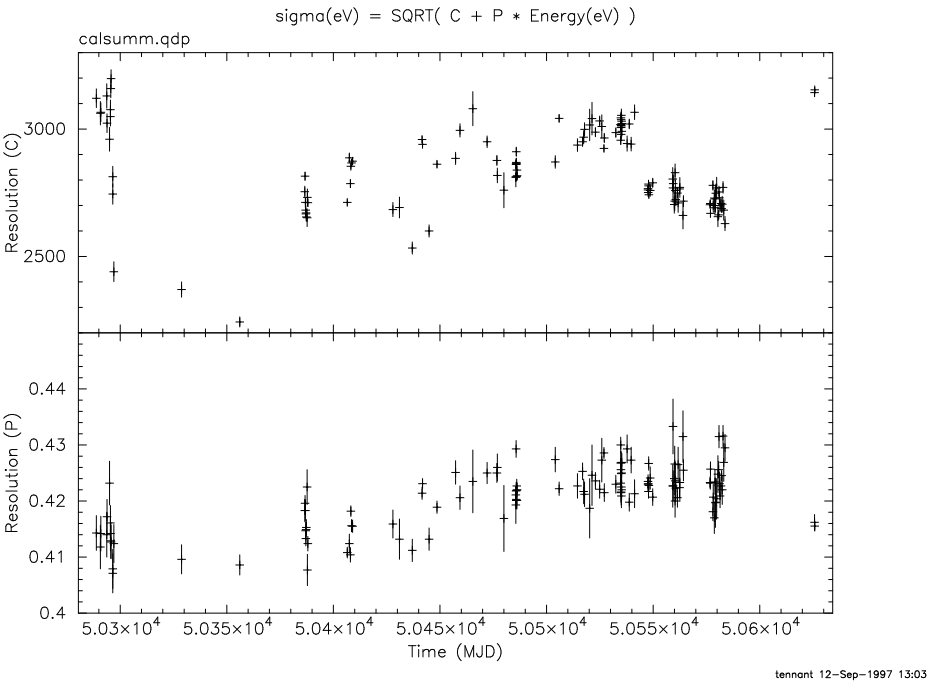

Figure 15: Temporal dependence of model resolution parameters.

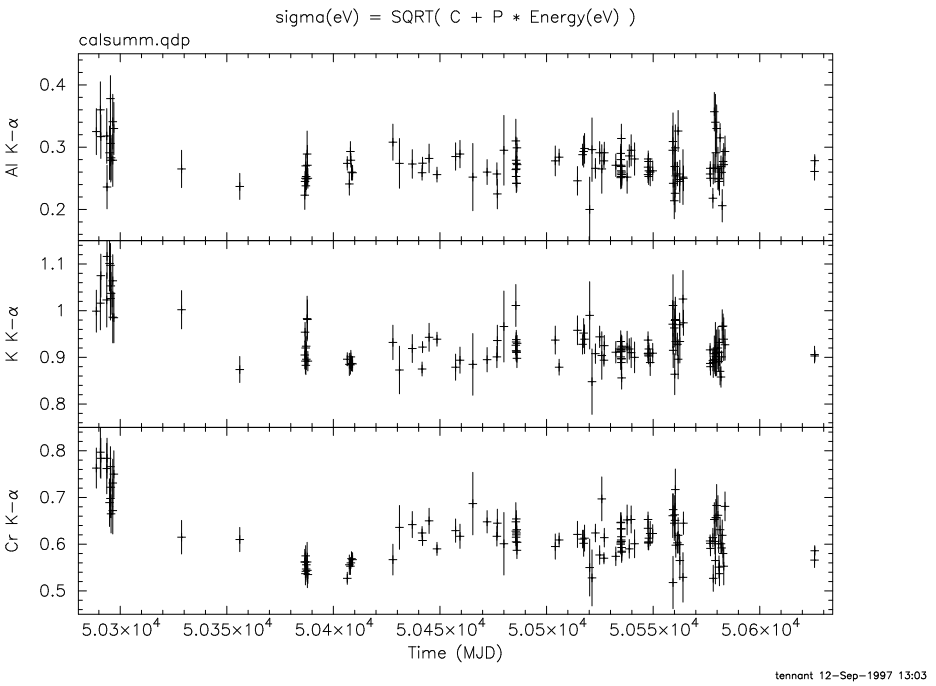

Figure 16: Temporal dependence of modeled line strengths for several lines, showing no significant time dependence.

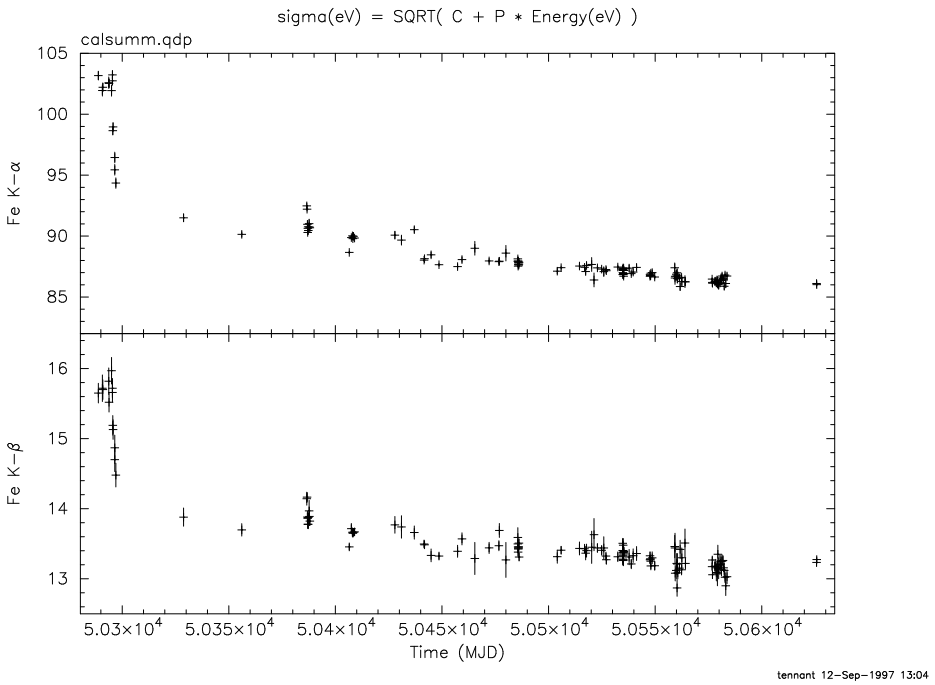

Figure 17: Temporal dependence of modeled line strengths for the Fe-K complex of lines.

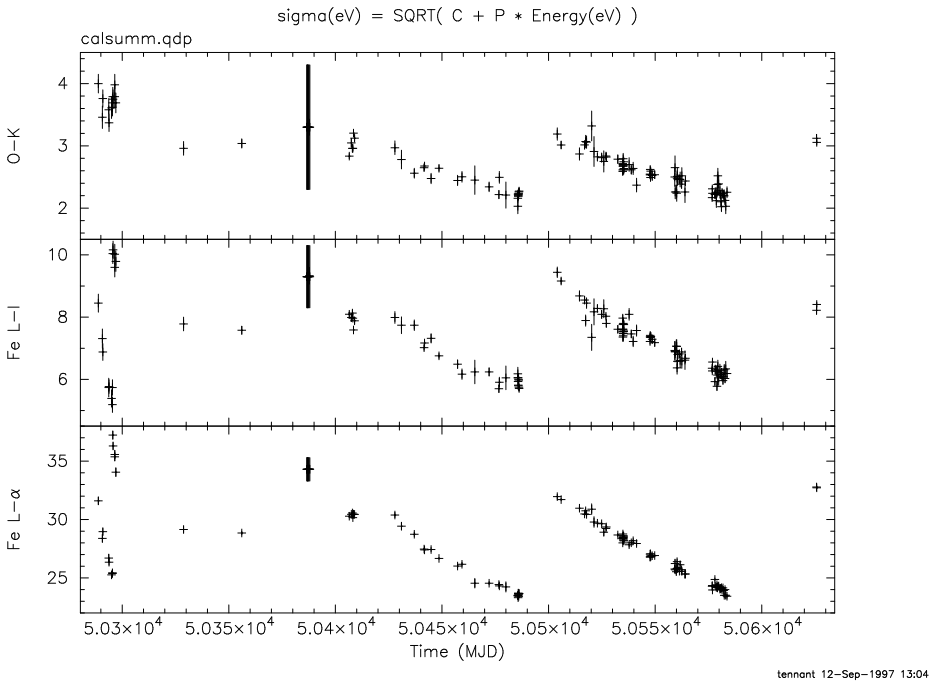

Figure 18: Temporal dependence of modeled line strengths for the Fe-L and O-K complex of lines.

3.2 Procedures

To fit the PHA spectra, we employed a model defined with the following PLT/COD function, using line energies from Reference [16]:

```
! P1,P2 gain offset slope
! P3,P4 resolution parameters
! p5  norm of O K
! p6  norm of Fe LIII-l
! p7  norm of Fe LIII-alpha
! Line energies:
VAR eOK        524.9 eOK     STO
VAR eFeL3l     615.2 eFeL3l  STO
VAR eFeL2e     628.  eFeL2e  STO
VAR eFeL3a     705.0 eFeL3a  STO
VAR eFeL2b1    718.5 eFeL2b1 STO
VAR eFeL1b3    792.  eFeL1b3 STO
VAR eAlKa     1486.5 eAlKa   STO
VAR eKKa1     3313.8 eKKa1   STO
VAR eCrKa1    5414.7 eCrKa1  STO
VAR eFeKa     6403.8 eFeKa   STO
VAR eFeKb1    7058.0 eFeKb1  STO
!VAR eFeKb2    7108.1 eFeKb2  STO
!VAR eWLl      7387.8 eWLl    STO
!VAR eNiKa1    7460   eNiKa1  STO
!VAR ePbLa2   10449.5 ePbLa2  STO
!VAR ePbLa1   10551.5 ePbLa1  STO
VAR ePuLa2   14084.2 ePuLa2  STO
VAR ePuLa1   14278.6 ePuLa1  STO
VAR ePuLe    16333   ePuLe   STO
VAR ePuLb6   16498.3 ePuLb6  STO
VAR ePuLb2   17255.3 ePuLb2  STO
!VAR ePuLb4   17556.0 ePuLb4  STO
VAR ePuLb5   17950.6 ePuLb5  STO
VAR ePuLb1   18293.7 ePuLb1  STO
!VAR ePuLb3   18540.5 ePuLb3  STO
VAR ePuLg1   21417.3 ePuLg1  STO
!VAR ePuLg2   21725.1 ePuLg2  STO
VAR ePuLg3   21982.4 ePuLg3  STO
VAR ePuLg6   22150.2 ePuLg6  STO
! Ge K edge is at 11.104
!VAR eGeKa2    9855.3 eGeKa2  STO
!VAR eGeKa1    9886.4 eGeKa1  STO
! Best single escape energy is about 2/3's of distance from K-a2 to K-a1.
VAR eGeKesc   9874.  eGeKesc  STO
!VAR eGeLesc   1090.  eGeLesc  STO
! General variable
var Energy
!************************************************************************
! Subroutines:
! push channel on stack, return the Energy
! Assumes E=p1+chan*p2
: gain
p2 * p1 +
;
```

```
!*************
! Returns gaussian, push norm, width, energy onto stack
: ngaus
Energy RCL - over / dup * 2 / neg exp swap / * 2.50663 / P2 *
;
!*************
! Assume Energy is on stack, return SSD resolution
! Uses sigma = SQRT(P4*E+P3)
: ssdres  P4 * P3 + SQRT ;
!*************************************************************************
: calsp
x gain Energy STO
0.0
 P5  eOK     RCL DUP ssdres SWAP ngaus +
 P6  eFeL3l  RCL DUP ssdres SWAP ngaus +
 P7  eFeL3a  RCL DUP ssdres SWAP ngaus +
 P8  eAlKa   RCL DUP ssdres SWAP ngaus +
 P9  eKKa1   RCL DUP ssdres SWAP ngaus +
P10  eCrKa1  RCL DUP ssdres SWAP ngaus +
P11  eFeKa   RCL DUP ssdres SWAP ngaus +
P12  eFeKb1  RCL DUP ssdres SWAP ngaus +
P13  ePuLa2  RCL DUP ssdres SWAP ngaus +
P14  ePuLa1  RCL DUP ssdres SWAP ngaus +
P15  ePuLe   RCL DUP ssdres SWAP ngaus +
P16  ePuLb6  RCL DUP ssdres SWAP ngaus +
P17  ePuLb2  RCL DUP ssdres SWAP ngaus +
P18  ePuLb5  RCL DUP ssdres SWAP ngaus +
P19  ePuLb1  RCL DUP ssdres SWAP ngaus +
P20  ePuLa2  RCL eGeKesc RCL - DUP ssdres SWAP ngaus +
P21  ePuLa1  RCL eGeKesc RCL - DUP ssdres SWAP ngaus +
P22  ePuLe   RCL eGeKesc RCL - DUP ssdres SWAP ngaus +
P23  ePuLb6  RCL eGeKesc RCL - DUP ssdres SWAP ngaus +
P24  ePuLb2  RCL eGeKesc RCL - DUP ssdres SWAP ngaus +
P25  ePuLb5  RCL eGeKesc RCL - DUP ssdres SWAP ngaus +
P26  ePuLb1  RCL eGeKesc RCL - DUP ssdres SWAP ngaus +
P27  ePuLg1  RCL eGeKesc RCL - DUP ssdres SWAP ngaus +
P28  ePuLg3  RCL eGeKesc RCL - DUP ssdres SWAP ngaus +
P29  ePuLg6  RCL eGeKesc RCL - DUP ssdres SWAP ngaus +
! Pulser parameters (ngaus in channel space)
P32 P31 P30 X - over / dup * 2 / neg exp swap / * 2.50663 /  +
! Line at specified energy
!P34  P33         DUP ssdres SWAP ngaus +
```

Figures 19 through 23 display sample ^{244}Cm spectra, with line identifications and model fits.

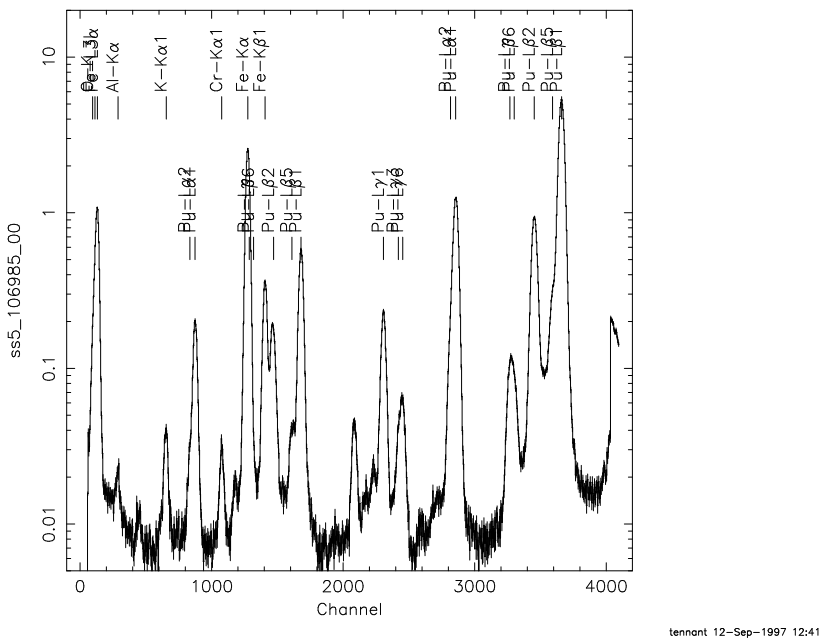

Figure 19: Spectrum of ^{244}Cm source obtained with SSD_5, showing model fit.

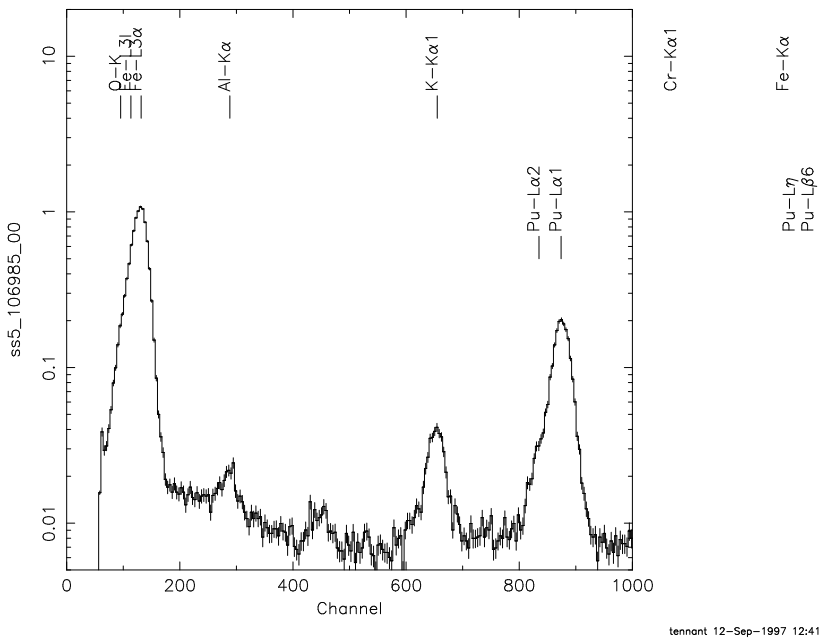

Figure 20: Low-energy spectrum of ^{244}Cm source obtained with SSD_5, showing model fit.

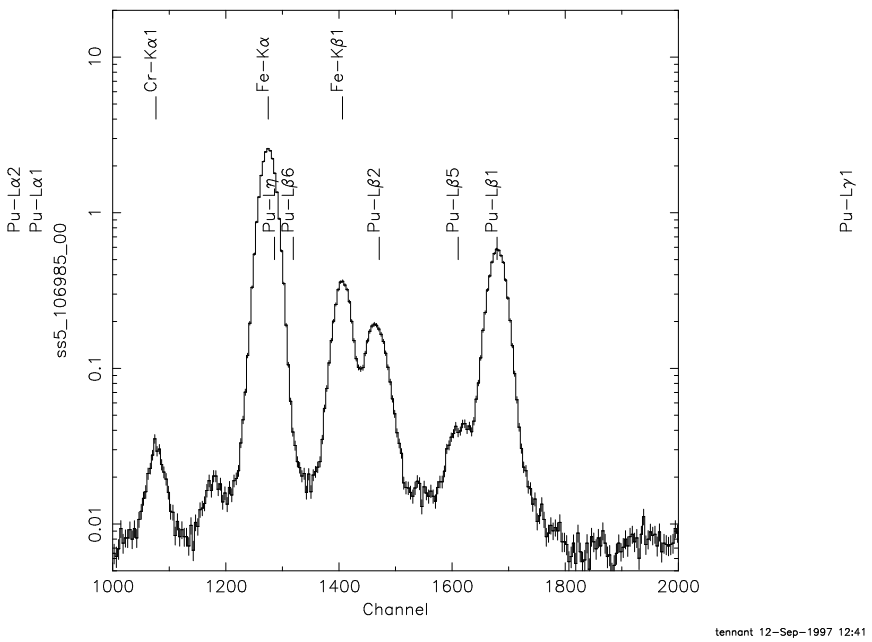

Figure 21: Spectrum near Fe-K lines of ^{244}Cm source obtained with SSD_5, showing model fit.

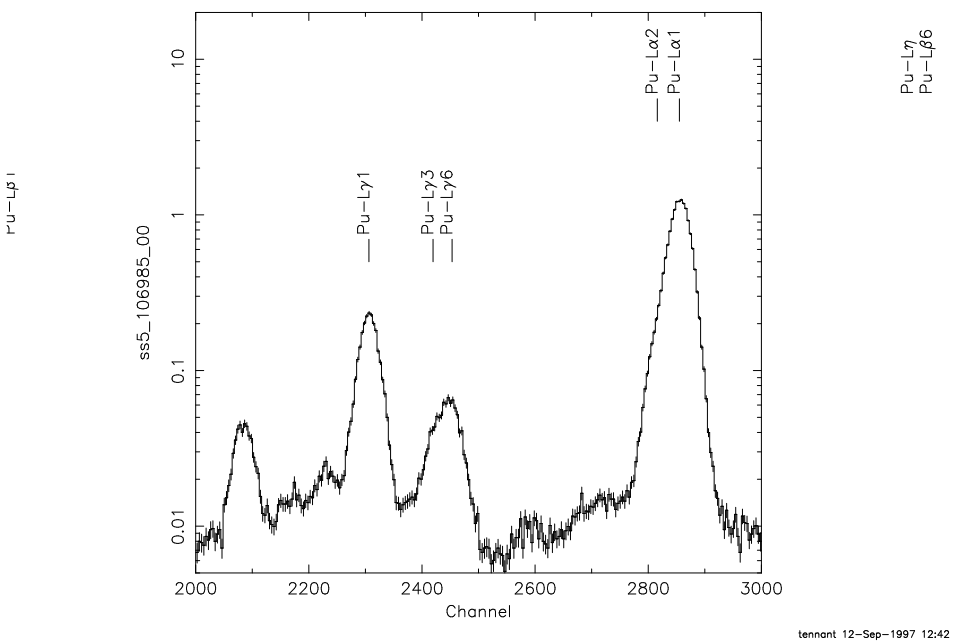

Figure 22: Medium-energy spectrum of ^{244}Cm source obtained with SSD_5, showing model fit.

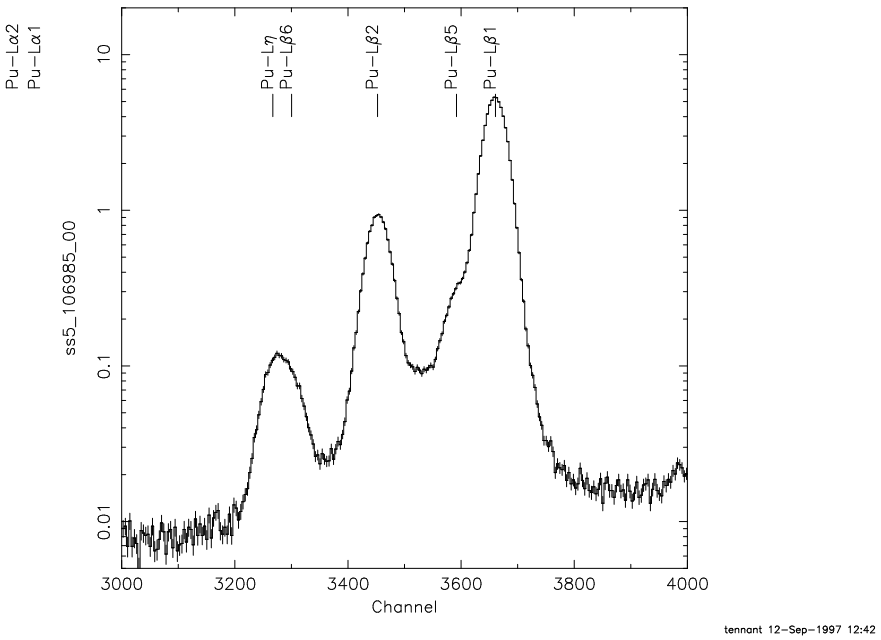

Figure 23: High-energy spectrum of ^{244}Cm source obtained with SSD_5, showing model fit.

3.3 Status

The most recent version, dated 1997-Aug-17, is currently in the QDP file `calsumm.qdp`. We plan to prepare an rdb table containing this information.

3.4 Data products

Currently, the data products for analysis of the SSD_5 internal calibration data are the QDP files `calsumm.qdp` and `calsumm.pco`. The latter (optional) file contains useful labels and a sensible default starting plot.

4 SSD continuum measurements

4.1 Effective area

4.1.1 Objectives

For calibrating the effective area, there are two complementary approaches:

1. Use a monochromatic source with no constraints on the detector's spectral resolution. Low-spectral-resolution detectors are adequate for this approach. However, it requires knowledge of the source's spectral purity (because a real source is not totally monochromatic) and samples only at discrete energies (thus requiring a model or interpolating scheme to span the spectral range).

2. Employ a continuum source with a detector having adequate spectral resolution. This approach simultaneously samples the entire spectrum at a spectral resolution proportionate to that of the detector. However, it requires knowledge of the detector's response matrix (because a real detector does not have a delta-distribution response).

4.1.2 Procedures

In principle, the methodology for calibrating effective area is straightforward. Expose two identical detectors, one a beam-normalization detector and the other a focal-plane detector at the focus of the optic, to a uniform beam of radiation. At a photon energy E, the effective area $A_{\rm eff}(E)$ of the optic's limiting aperture is approximately the following:

$$A_{\rm eff}(E) \approx \frac{C_{\rm fpd}(E) D^2_{\rm optic}}{C_{\rm bnd}(E) D^2_{\rm bnd}} A_{\rm bnd} \ . \tag{7}$$

Here, $C_{\rm fpd}(E)$ and $C_{\rm bnd}(E)$ are, respectively, the count rates (at energy E) in the focal-plane detector and the beam-normalization detector; $D_{\rm optic}$ and $D_{\rm bnd}$, the distances to the optic and BND; and $A_{\rm bnd}$, the area of the BND's aperture. Ideally, this approach would not need calibrated detectors, because the efficiencies of the *identical* detectors cancel in the count-rate ratio: Only the distance ratio and the area of the beam-normalization detector's aperture require absolute calibration. Of course, the accuracy of this approximation (Eq. 7) depends on the extent to which the detectors' response matrices are identical (or cross-calibrated) and upon knowledge of the beam's uniformity. Furthermore, the approximation is accurate only if (a) the radiation is spectrally pure or (b) the detector's spectral resolving power is high.

The ultimate calibration of the absolute effective area will not use the simple ratio in Equation 7. Instead, parameter optimization through forward fitting measured pulse-height-amplitude (PHA) spectra with simulated spectra will determine the effective area. *The model is the calibration.*

Here we use Equation 7 for a preliminary calibration of the effective area of HRMA mirror shells, using measurements of continuum spectra with the HXDS's BND and focal-plane SSDs — SSD_5 and SSD_X. For these effective-area measurements, the EIPS (§1.1.1) served as an x-ray-continuum source, with a C target at 15 kV and a Be transmission filter. Because the detectors' gains are not perfectly matched, it is necessary to fine-tune the energy scale: The presence of weak lines facilitates this minor adjustment, made before taking the ratio of the PHA spectra.

Figure 24 exemplifies data used for shell 6. To the extent that SSD_5 and SSD_X are identical, the shell-6 effective area at the XRCF is simply the ratio of the SSD_X PHA spectrum to that of the SSD_5, appropriately scaled for distance ratio and BND's aperture (Eq. 7). Figure 25 summarizes the results for all 4 HRMA shells. One of the great advantages of this approach is apparent: A single measurement determines the effective area at all energies above about 1 keV, at the spectral resolution of the SSDs. Below about 1 keV, the data are unreliable, owing to a steep decline in SSD efficiency and to expected differences between SSD efficiencies resulting from slightly different windows and from differential accumulation of ice on the SSD windows.

To predict the effective area of each HRMA shell at the XRCF, we employ the MSFC Project Science ray-trace code. This code includes thermal pre- and post-collimators, central aperture plate, and as-built mirror element and shell parameters (SAO/ T. Gaetz, private communication), but no figure-error or

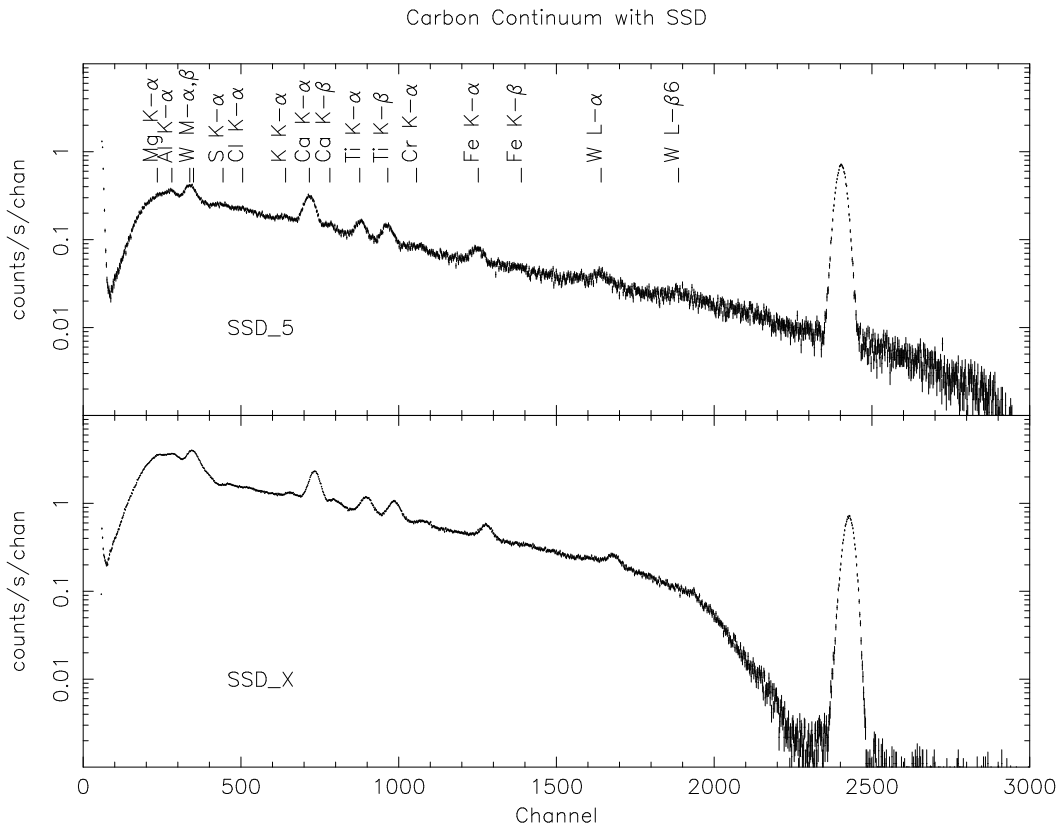

Figure 24: SSD-measured spectra for a carbon target at 15 kV, exhibits a smooth continuum with some relatively weak, atomic fluorescence lines from contaminants in the target. Top panel is the pulse-height-amplitude (PHA) spectrum for SSD_5; bottom, the PHA spectrum for SSD_X at the focal plane of shell 6. Each PHA spectrum shows the pulser (near channel 2400); the bottom one also displays a discrete drop at the (iridium) Ir-M_V edge (near channel 400) and a roll-over at the critical energy (near channel 2000) for the mirror-shell's mean grazing angle. (The energy scale is approximately 5 eV per channel.)

surface-roughness effects. Using a Monte-Carlo simulation, it records the position and direction of each ray at the nominal focal plane, plus the grazing angle upon reflection at each mirror surface. In post processing, a second program calculates the reflectance at each interface, for each ray stored during the Monte-Carlo simulation, using the optical constants of the mirror coating (iridium). Above 2 keV, we use constants [17] derived from synchrotron studies [18, 19] (SAO/ D. Graessle, private communication); below 2 keV, we employ tabulated values [20] (see `http://www-cxro.lbl.gov/optical_constants`). Away from edges, the synchrotron data reproduce the Henke et al. [20] data above 2 keV, after adjusting the latter to an iridium density of 0.9725 bulk. Thus, the reflectance computations below 2 keV assume this density for a uniform iridium coating. The MSFC code gives effective-area results in agreement with those from the independent SAO ray-trace model (SAO/ D. Jerius, private communication).

To compare with the effective area empirically determined through continuum measurements with the SSDs, we next convolve the ray-trace-model effective areas with a gaussian of 0.21 keV Full-Width at Half-Maximum (FWHM), representative of the SSD's spectral resolution. Furthermore, because the focal-plane SSD measurements employed a 2-mm-diameter aperture, we decrease the predicted effective areas (over the entire focal plane) by the expected fraction of flux scattered outside the aperture. To calculate this fraction, we use the spatial power spectral densities, determined from pre-coating metrology, averaged over axial and azimuthal position for each mirror (SAO/ T. Gaetz, private communication). For shells 3, 4 and 6, this procedure gives excluded flux fractions similar to those predicted by the SAO

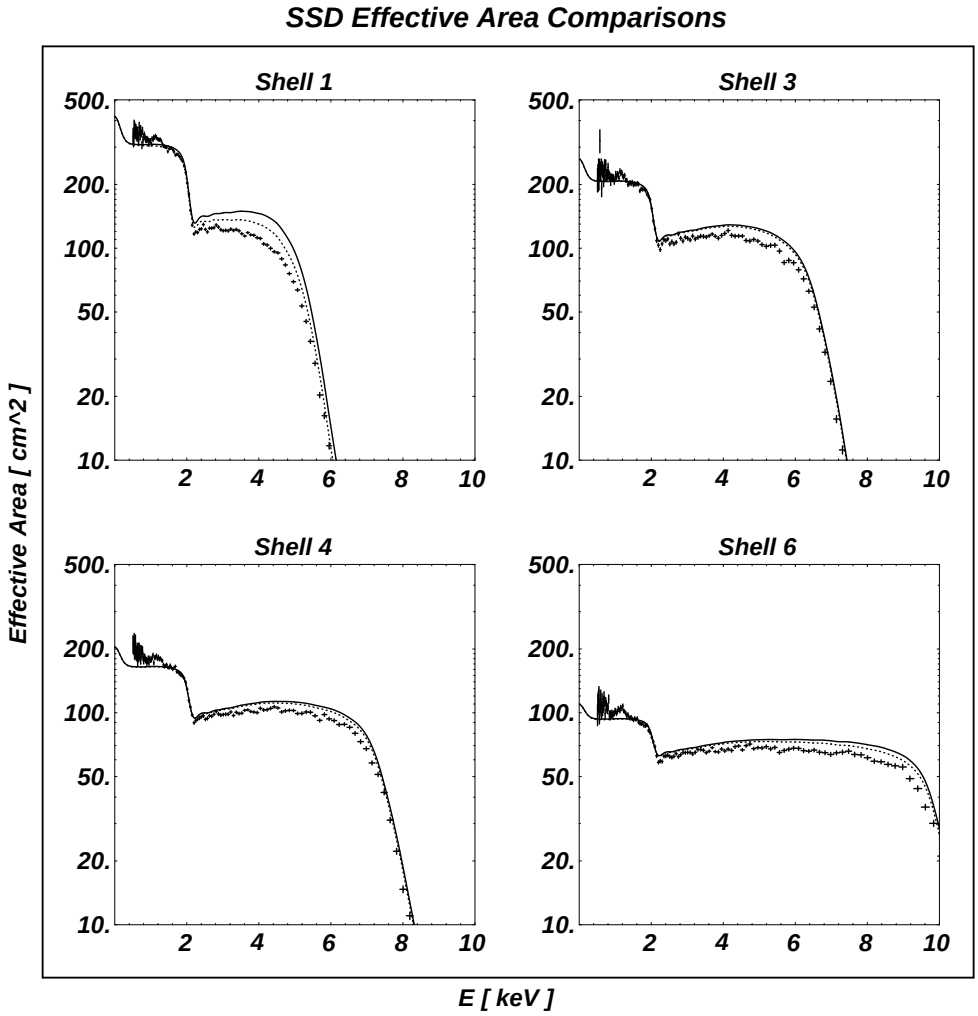

Figure 25: Comparison of measured with predicted effective area of each HRMA shell shows a discrepancy of about 10%. Data are the quotient of the focal-plane detector's pulse-height-amplitude (PHA) spectrum by the corresponding beam-normalization detector's PHA spectrum, scaled by the distance-ratio squared and the BND's aperture area. The solid line denotes the model prediction for the effective area over the entire focal plane; the dotted, over a 2-mm-diameter (40-arcsec) focal-plane aperture.

scattering model (SAO/ D. Jerius, private communication). However, for shell 1 this procedure predicts an excluded flux fraction that rises more sharply with energy than that predicted by the SAO model.

Even after the correction for scattering, the predicted effective areas exceed the SSD-measured values (Fig. 25) by about 10%. These results are preliminary: A full analysis awaits complete characterization of the SSD response and completion of the SAO synchrotron reflectivity program [18]. In addition, we are exploring the consequences of lower iridium densities [21], finite thickness for the iridium and (binding-layer) chromium coatings (unimportant at or below the critical energy), density gradients at the surface of the iridium layer, and surface roughness. We shall also include effects due to molecular [22, 23] or particulate [24, 25] contamination; however, based on AXAF's very stringent contamination-control program and analyses of optical witness samples, we do not expect these effects to be significant.

4.1.3 Status

Preliminary work is complete, however, dead-time corrections are the next necessary step. We shall repeat the analysis after the SSDs are calibrated and then perform a forward-modeling analysis.

4.1.4 Data products

Figure 25 shows both measured and predicted results. Corresponding data will be accessible from the Project Science Calibration web page `http://wwwastro.msfc.nasa.gov/xray/xraycal/cat.html`.

4.2 Alignment

4.2.1 Objectives

Five ground-support actuators provide fine positioning of the HRMA (§1.1.3) in the XRCF Instrument Chamber (IC): The specified precision for controlling pitch and yaw is 10 arcsec. A laser system enables initial alignment of the HRMA Alignment Reference Mirror (ARM) to the XRCF Facility Optical Axis (FOA), to a tolerance of 10 arcsec. Although the HRMA's effective area and point-response function are insensitive to misalignment on these scales, it is nonetheless necessary to verify the alignment in x rays, particularly for examining off-axis effects. Here, we describe an effective and efficient x-ray alignment test, discuss its sensitivity, and report results of the test.

We note that x-ray verification of alignment was not routine. Initial attempts to confirm alignment, by comparing line count rates through opposite shutters, failed due to an unanticipated small decenter of each HRMA hyperboloid relative to its corresponding paraboloid. However, the x-ray-continuum alignment test, described here, is relatively insensitive to decenter, thus allowing an unequivocal verification of the HRMA's alignment to the XRCF FOA.

4.2.2 Procedures

The HRMA ground-support equipment included a shutter system, shown schematically in Figure 26, which can isolate any combination of the HRMA's 16 shell quadrants. The principal applications for the shutters were in determining best focus ("shutter focus"), in measuring paraboloid-to-hyperboloid tilt [26], and in performing subaperture measurements of the point spread function (PSF).

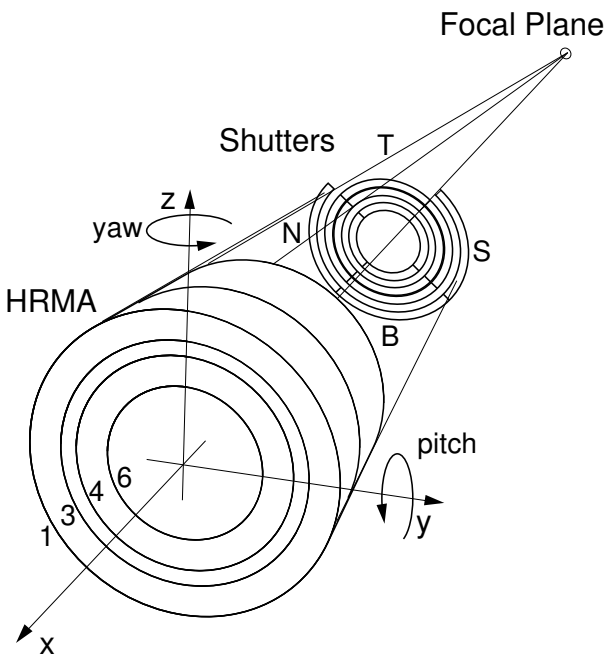

Figure 26: An assembly of 16 independent shutters isolates the converging x-ray beam of each quadrant (T=top, N=north, B=bottom, and S=south) of the HRMA's 4 mirror shells (1, 3, 4, and 6). Arrows indicate positive directions of the XRCF coordinate axes and HRMA pitch θ_y and yaw θ_z. The displayed shutter configuration has the top (T) quadrant of shell 1 open and all others closed.

A very sensitive test of alignment for grazing-incidence optics is the azimuthal dependence of the critical energy at which the mirror's response plummets. Using the HRMA shutters, we determined this critical energy for each shell quadrant. To do this efficiently, we used the HXDA focal-plane SSD [5], SSD_X (§1.1.5) to measure EIPS [2] continuum radiation (§1.1.1). By comparing the SSD_X spectrum observed through one shell quadrant with that through the opposite quadrant, we establish the alignment of that shell in the plane passing through the quadrant centers. Specifically, we divide the SSD_X PHA spectrum for continuum x rays through one shell quadrant by that through the opposite quadrant.

For estimating this effect, we constructed a simple 2-dimensional model and compared it with predictions from the MSFC Project Science HRMA ray-trace code (4.1.2). Both took into account the finite source distance (528 m at the XRCF), which results in grazing angles for the paraboloid (hyperboloid) being greater (less) than the infinite-conjugate values by 3.6, 2.9, 2.5, and 1.9 arcmin (quadrant averaged) for shells 1, 3, 4, and 6, respectively). Both predict the same sensitivity dependence, which is slightly stronger than that observed. Figure 27 shows that the ratio of PHA spectra from opposite quadrants is quite sensitive to misalignment: E.g., a 1-arcmin misalignment results in a ratio of nearly 2 near the critical energy (9.9 keV for HRMA shell 6).

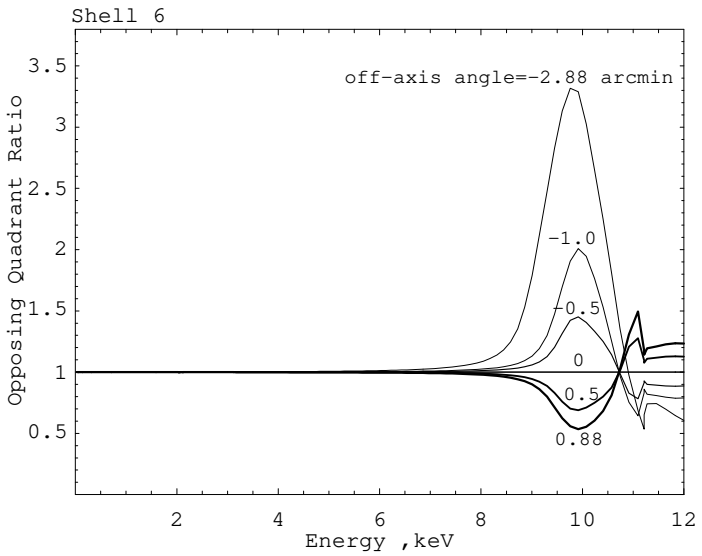

Figure 27: The ratio of quadrant throughput near the critical energy is a sensitive function of off-axis angle. This plot shows that the ratio of SSD_X PHA spectra for opposing quadrants of HRMA shell 6 can detect even relatively small (0.1 arcmin) misalignment.

Figure 28 exhibits the ratio of SSD_X PHA spectra for opposing quadrants, for the other 3 HRMA shells. As shell diameter and, hence, mean grazing angle increase, the critical energy decreases and the sensitivity diminishes. Indeed, HRMA shell 1 requires a 4.5-times-larger off-axis angle than shell 6, to achieve a PHA ratio of 2. This decreased sensitivity occurs (a) because a given misalignment angle is a smaller fraction of the mean grazing angle and (b) because the grazing-angle cut off becomes less steep as the reflectance is more lossy at lower energies.

X-ray verification of HRMA alignment employed data for individual shell quadrants, at several off-axis angles. For ease of analysis, we binned SSD_X's 4096 PHA channels into blocks of 32. To normalize, we summed the SSD_5 PHA spectrum over the range 1.44–7.2 keV and then divided this into the SSD_X PHA spectrum. Next, for a given HRMA shell and off-axis angle, we divided bin-by-bin the normalized SSD_X spectrum for one quadrant by that for the opposite quadrant. Using observed atomic lines, we monitored the SSD gain and found no significant variation.

The x-ray alignment verification probed 6 yaw and 3 pitch angles for shell 6. Figure 29 shows that the maximum PHA ratio was well above 3 at the largest yaw angle, but unity at the putative on-axis position. Figure 30 shows similar results for the pitch dependence. These results verify, in x rays, that the laser alignment of the HRMA ARM to the XRCF FOA was correct. Figure 31 exemplify results for

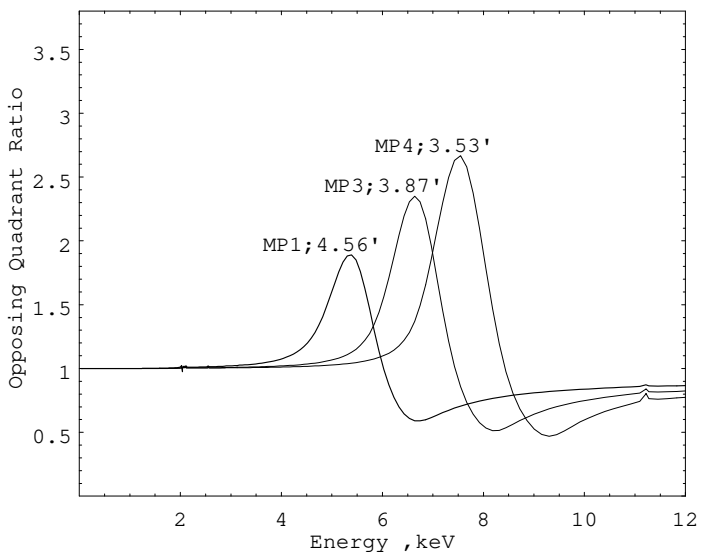

Figure 28: The sensitivity to off-axis angle, of the ratios of PHA spectra for opposing quadrants is smaller for the outer mirror shells. This plot displays expected curves for each shell's extreme off-axis measurements.

the other HRMA shells, displaying results at the extreme yaw for each shell. The decrease in the ratio with larger shells is again consistent with expectations.

For each shell and off-axis angle, we reduced the PHA ratio to a single value, by summing over the region of interest (ROI) for which the response is most sensitive to off-axis angle — namely, 4.8–5.92, 6.24–7.36, 7.04–8.16, and 9.28–10.4 keV, for HRMA shells 1, 3, 4, and 6, respectively. In addition, we summed over a reference ROI (2.4–3.52 keV) and divided this into the sum over the sensitive ROI. Next, we divided the values for opposite quadrants to obtain a single scalar ratio for each measurement pair. Then, we performed the same manipulations for the simple model and compared the measured with model values in a scatter plot (Fig. 32). Finally, we applied a linear fit to $R_{\rm observed} = mR_{\rm model} + b$, resulting in the best-fit curve shown in the Figure 32.

The best-fit parameter values and 1-sigma errors are $m = 0.713 \pm 0.014$ and $b = 0.281 \pm 0.013$. The departure of m from unity, and b from zero indicate the simplicity of the model or the analysis and, for now, prevents this method from quantitatively determining the off-axis positioning accuracy.

The quantity $m+b$ is more interesting, because many sources of systematic errors cancel in the ratios. If the commanded on-axis position is really on-axis, then the observed ratio should be 1 as expected, constraining $m + b$ to unity as well. The best-fit value is $m + b = 0.994$, with a 95% confidence interval ranging from 0.972 to 1.016. This corresponds to a 95% confidence interval for HRMA alignment to the FOA of -2.4 to 4.1 arcsec. We thus infer that the ARM, the HRMA, and the XRCF were all aligned within this angular range when on-axis.

The χ^2 for the fit was 55.0 with 25 degrees of freedom; however, we assumed no uncertainty for the commanded HRMA position. Applying the formula $\delta R = \delta\theta(dR/d\theta)$, where R is the ratio and θ is the off-axis angle, to each expected value then limits the value of $\delta\theta$. The value of $\delta\theta$ required to obtain a χ^2 which is 50% probable for a linear fit to the data in Figure 32 is 6 arcsec. Under the assumption that errors in the commanded position are the only additional source of error, the 95% confidence interval for $\delta\theta$ ranges from 2 to 11 arcsec.

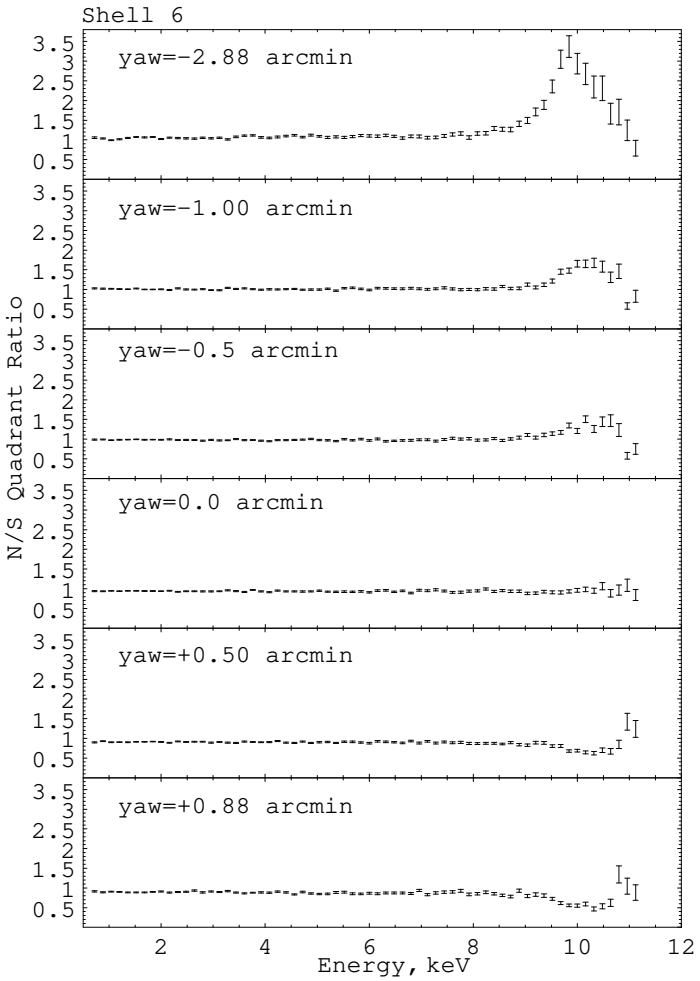

Figure 29: Ratios of normalized, binned PHA spectra for measurements with north (N) and south (S) shell-6 shutters open illustrate test's sensitivity to yaw and verify alignment of HRMA to FOA in yaw.

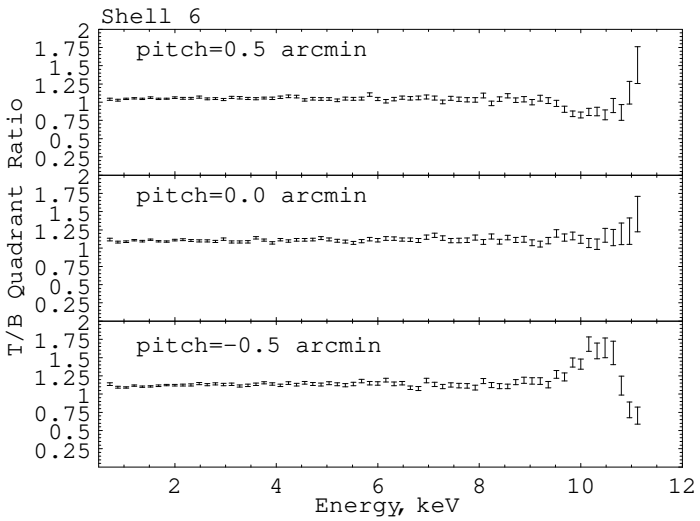

Figure 30: Ratios of normalized, binned PHA spectra for measurements with top (T) and bottom (B) shell-6 shutters open illustrate test's sensitivity to pitch and verify alignment of HRMA to FOA in pitch.

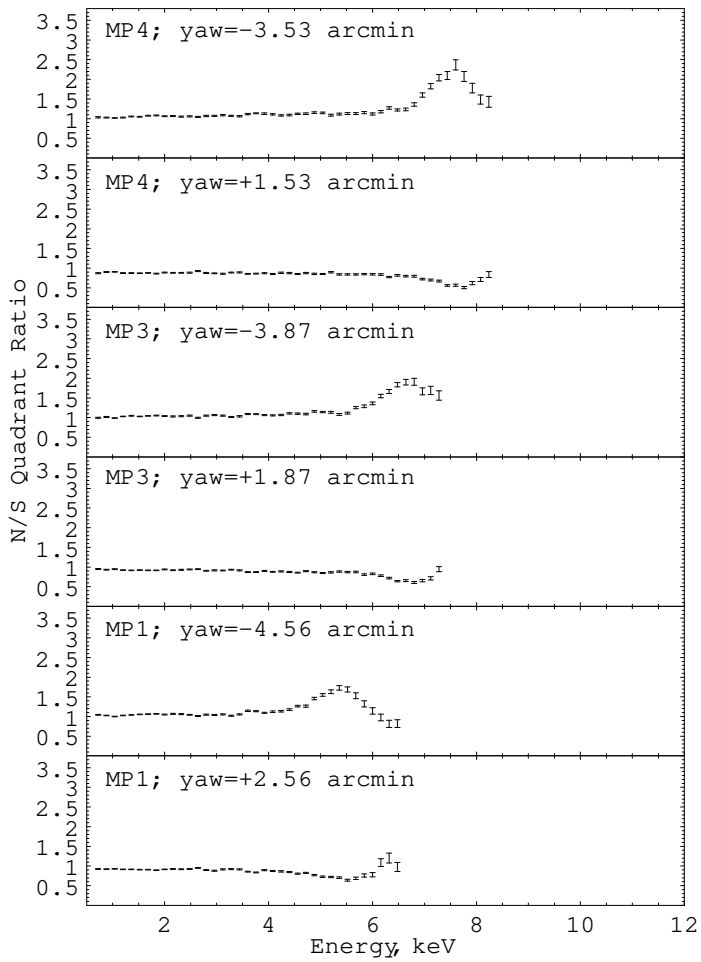

Figure 31: Ratios of normalized, binned PHA spectra for measurements with north (N) and south (S) shutters open illustrate test's sensitivity to yaw for HRMA shells 1, 3, and 4. This plot shows the PHA ratios at the extreme off-axis angles tested for each HRMA shell.

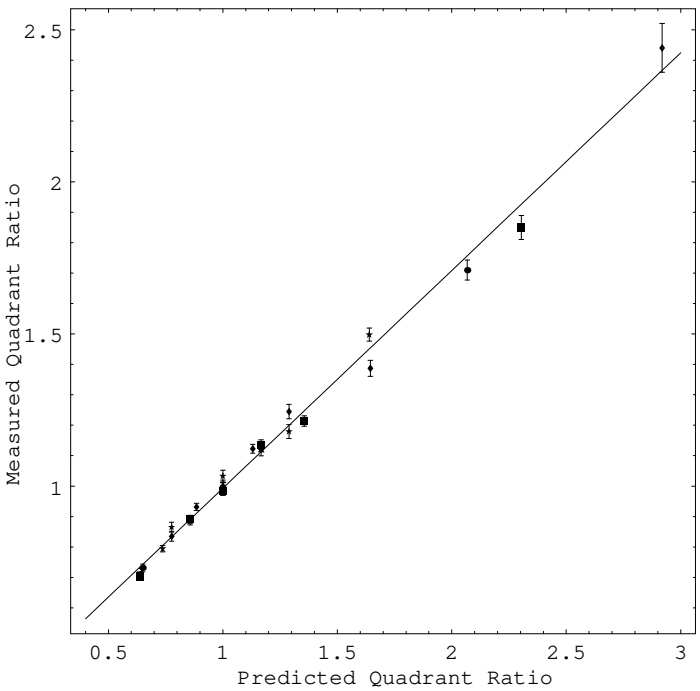

Figure 32: A comparison of measured versus fitted PHA ROI ratios, combining all measurements of pitch and of yaw, for all mirror shells, shows fair agreement with the model predictions, after scaling by about 0.7.

5 Flight Contamination Monitor

5.1 Objectives

There are two objectives of the ground and in-orbit measurements using the Flight Contamination Monitor (FCM) and focal-plane detectors (ACIS and, on the ground only, ACIS-2C and HRC-I):

1. Verify the transfer of the HRMA flux scale from XRCF test phase to orbital-activation phase.

2. Measure or bound any changes in molecular contamination of the HRMA [3].

Note that the focal-plane detectors also employ their own radioactive calibration sources, in order to monitor any change in detector performance.

5.2 Procedures

5.2.1 Source characterization

The FCM comprises 16 (1 per shell quadrant) electron-capture sources, containing ^{109}Cd and ^{55}Fe prepared at Isotopes Products, packaged by MSFC, and mounted on the Forward Contamination Cover (FCC). Because of leakage, MSFC sealed each source assembly with a 100-μm-thick beryllium window (MSFC/ B, Ramsey 1997, private communication). MSFC also measured source activities, with corroborating measurements by the US Army Redstone Arsenal (MSFC/ B, Ramsey 1997, private communication). Based on these measurements, we then used a Monte-Carlo simulation to determine emission rates in the forward direction (Ramsey 1997, private communication) for all fluorescence lines. Eastman-Kodak Company (Tech Note AXAF-96-0251-SCHWAB) determined source positions on the FCC.

5.2.2 Forward Contamination Cover (FCC) registration

The arrangement of sources on the FCC mitigates variations in the detected rates due to displacement of the FCC. Nevertheless, for comparison of ground and orbital measurements, it is necessary to register the measured FCC image by comparing it with a simulated image, to search for positional shifts. For example, the FCM sources will shift position slightly due to FCC thermal contraction in the colder on-orbit environment. The registration procedure is straighforward centroiding of the measured images by fitting to crossed gaussians and comparison with centroiding of simulated images for various FCC displacements and distortions. To do this, we must first establish the position of the optical axis in focal-plane detector coordinates. Tools for this analysis include software for handling FITS images, our ray-trace code, and Mathematica^{TM} notebooks.

5.2.3 Spectral content

The flux-scale transfer requires measuring the line strengths, primarily of Ag-L (from ^{109}Cd electron capture) and Mn-K (from ^{55}Fe electron capture) lines, first at the XRCF and then in orbit, adjusting for any displacement or shrinkage of the FCC and any changes in the ACIS quantum efficiency. Because the analysis requires knowledge of the ACIS response as a function of position as well as energy, we must incorporate results from ACIS flat-field measurements at the XRCF. Also required are proper treatment of telemetry drop-out, pile-up, etc. Changes in HRMA molecular contamination would alter the detected strengths of the lines, especially the Ag-L lines just above the Ir-M$_V$ edge. Prediction of detected line strengths — using source simulations, ray trace, and convolution with detector response — permits evaluation of the flux-transfer procedure.

5.2.4 Contamination and flux scale

The spectral analysis, combined with simulations, will allow us to determine or bound any changes in HRMA molecular contamination or flux scale.

5.3 Status

5.3.1 Source characterization

Table 6 lists average measured activities per FCM source, by shell. Dominated by systematic effects, estimated errors are ∼15%. Although predicted absolute rates for lines arising from electron capture are no more accurate than the activity measurements, relative rates should be as accurate as the tabulated branching ratios [27] — i.e., a few %. Predicted rates, absolute or relative, for fluorescent lines excited in the source and its holder, primarily by Ag-Kα and Mn-Kα lines, are much less secure owing to complexity of the simulations and number of interaction pathways (MSFC/ B. Ramsey 1997, private communication). Because the radioactive half-lives of ^{109}Cd and ^{55}Fe are 1.2665 ± 0.0011 and 2.73 ± 0.03 yr, respectively, it is necessary to compensate for exponential decay of the source activities.

Table 6: Average FCM activities (mCi) per source for 1997 March 5.

Shell	1	3	4	6
^{109}**Cd**	3.8	2.3	1.5	0.68
^{55}**Fe**	0.95	0.79	0.48	0.24

5.3.2 Forward Contamination Cover (FCC) registration

Figure 33 shows a simulated focal-plane image of the FCM, overlaid with outlines of the focal-plane detectors (for ACIS-S and HRC-I aim points). Although the image's global topology is independent of energy, the contours depend slightly upon energy due to different responses of the 4 HRMA shells.

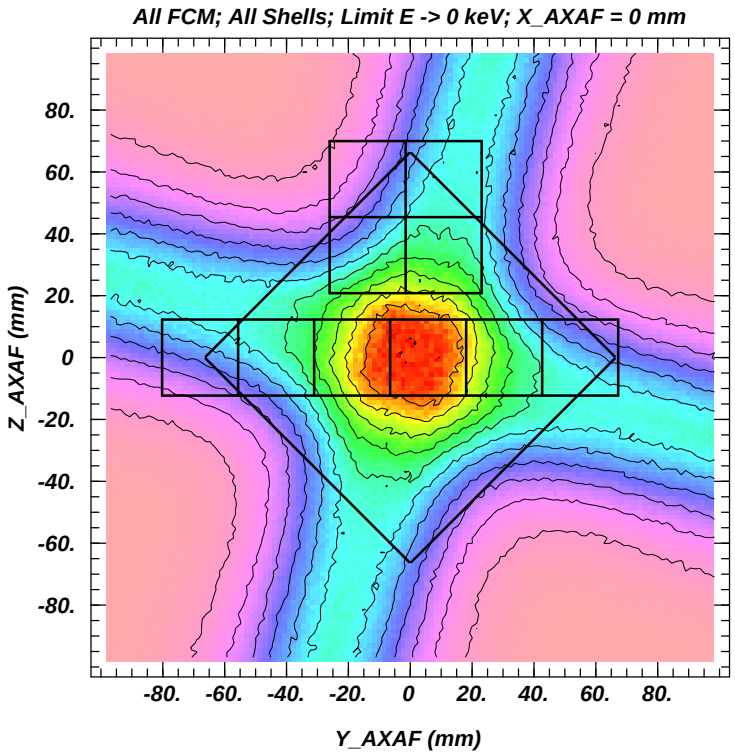

Figure 33: Simulated focal-plane image of FCM, with outlines of AXAF detector focal planes.

Initial XRCF FCM measurements used the HRC-I. Figure 34 compares a simulated HRC-I image of the FCM at zero displacement from its nominal position, with the actual image obtained at the XRCF. As shown in Figure 35, centroiding indicates a 0.75-mm displacement in $Y_{\rm AXAF}$ of the FCC from its nominal position. We shall perform a similar centroiding analysis for each FCM measurement with ACIS-2C and ACIS at the XRCF, and with ACIS in-orbit. Figure 36 shows an ACIS image of the FCM obtained at the XRCF.

5.3.3 Spectral content

The primary analysis monitors changes in detected line rates between the XRCF and on-orbit measurements. Also of interest is a comparison of these rates with predicted ones, which would add confidence to our understanding of the sources, HRMA, and detector. Figure 37 shows preliminary results for detected line rates for amplifier 0 of back-illuminated (BI) CCD S3; Figure 38, for amplifier 0 of front-illuminated (FI) CCD S2. The spectra represent ∼1 hour of data, taken on Day 116 of calibration at the XRCF. Using `PHAPLT` and appropriate energy resolution models, and including all grades, we determined these rates. Ag-L and Mn-K lines, as well as Au-M lines (from the source's gold overcoat), show up clearly. The superior energy resolution of the front-illuminated chips over the back-illuminated ones is evident in these spectra (cf. Figs. 37 and 38).

Thus far, we have not modeled even the strong Ag-L and Mn-K lines as well as desired. Hence, we need more accurate modeling of the ACIS response and of the line complexes.

For the data described above, Table 7 lists the count-rate ratios of the Ag-L line complex to those in Mn-Kα line, for each amplifier in each of 6 CCDs. Significant variation in this ratio appears from chip to chip, indeed from amplifier to amplifier. Because we expect some variation due to the energy dependence of the FCM image contours, we require ACIS flat-field data and detailed simulations, in order to extract line rates and ratios sufficiently accurate to bound molecular contamination and flux-scale changes.

Table 7: FCM (Ag-L$\alpha\beta\gamma$/Mn-Kα) count-rate ratios (all grades) for active ACIS CCD amplifiers

CCD	Amp	Ratio	Error	CCD	Amp	Ratio	Error
0 (I0)	0	0.895	0.047	3 (I3)	0	0.536	0.011
0 (I0)	1	0.851	0.040	3 (I3)	1	0.549	0.013
0 (I0)	2	0.801	0.034	3 (I3)	2	0.543	0.012
0 (I0)	3	0.810	0.031	3 (I3)	3	0.517	0.012
1 (I1)	0	0.500	0.012	6 (S2)	0	0.526	0.012
1 (I1)	1	0.519	0.012	6 (S2)	1	0.512	0.011
1 (I1)	2	0.519	0.012	6 (S2)	2	0.483	0.010
1 (I1)	3	0.459	0.012	6 (S2)	3	0.451	0.008
2 (I2)	0	0.859	0.029	7 (S3)	0	0.595	0.018
2 (I2)	1	0.751	0.022	7 (S3)	1	0.615	0.020
2 (I2)	2	0.695	0.018	7 (S3)	2	0.611	0.020
2 (I2)	3	0.594	0.014	7 (S3)	3	0.650	0.023

5.3.4 Contamination and flux scale

As yet, we have no results to report on contamination and the flux scale.

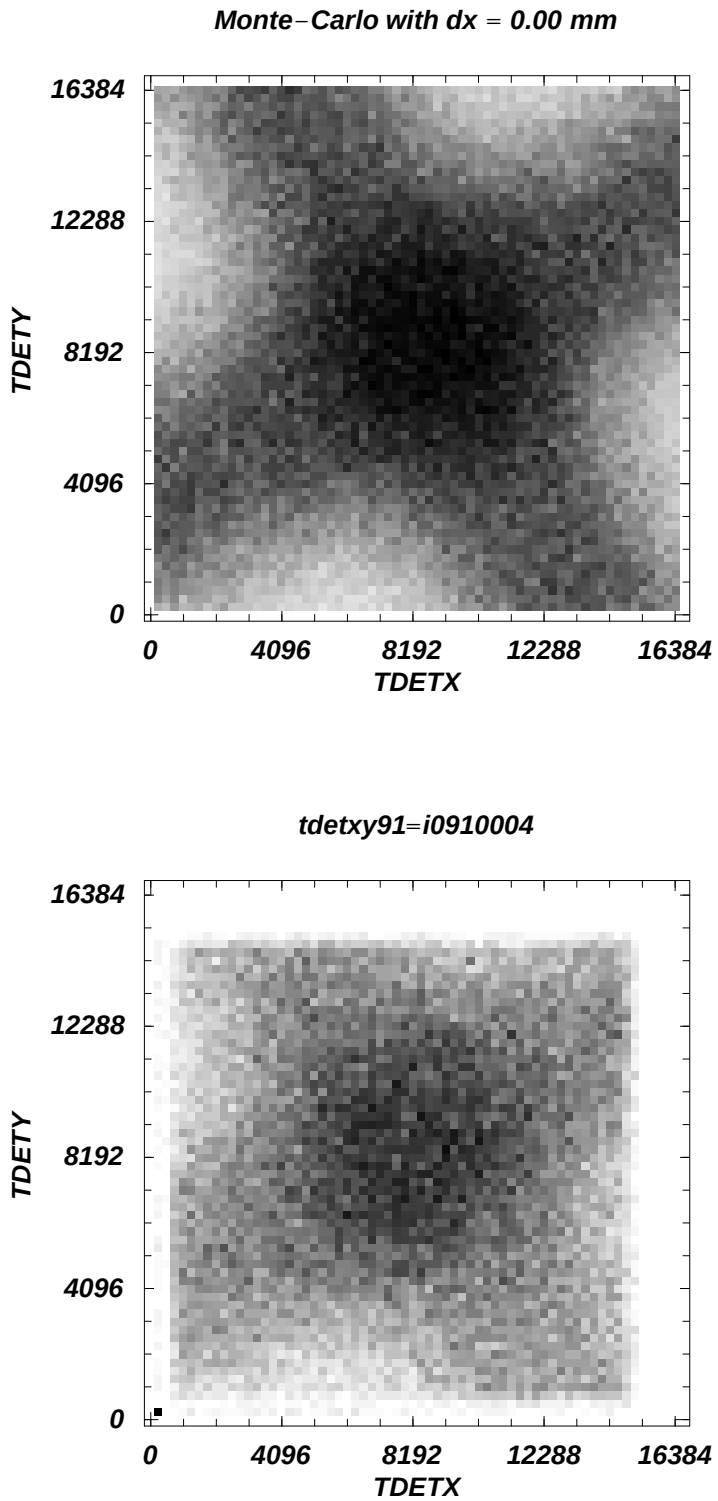

Figure 34: Comparison of simulated and measured HRC-I images of FCM, both in detector coordinates. Top panel shows a simulated HRC-I FCM image; bottom, a measured one obtained on Day 91 of calibration at the XRCF.

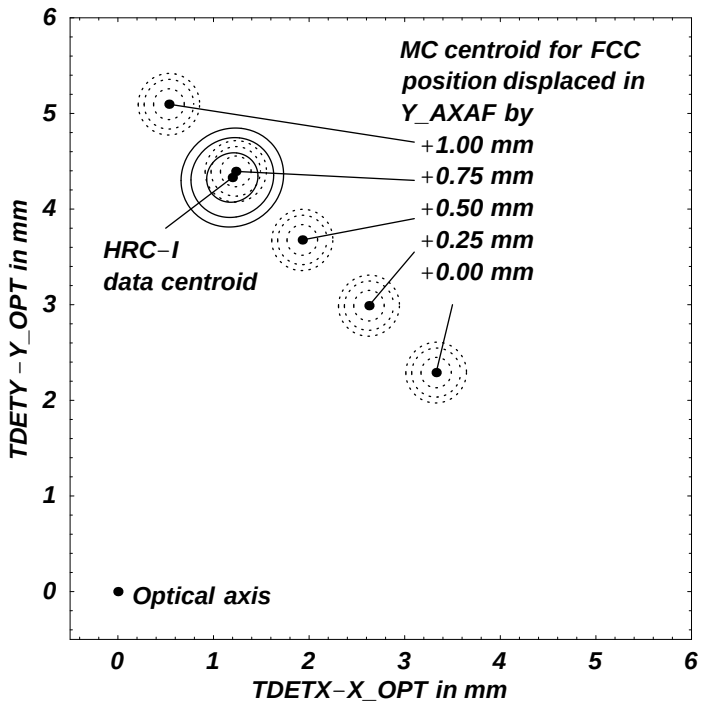

Figure 35: Comparison of measured centroid of HRC-I image of FCM with centroids of simulated images suggests a 0.75-mm FCC displacement in Y_{AXAF}.

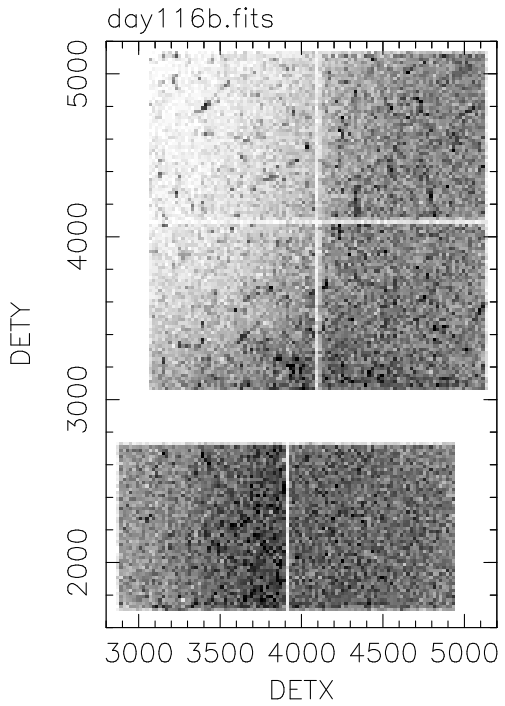

Figure 36: ACIS FCM image, in detector coordinates, taken on Day 116 of calibration at XRCF. Approximately 1 hr of data are included in this image.

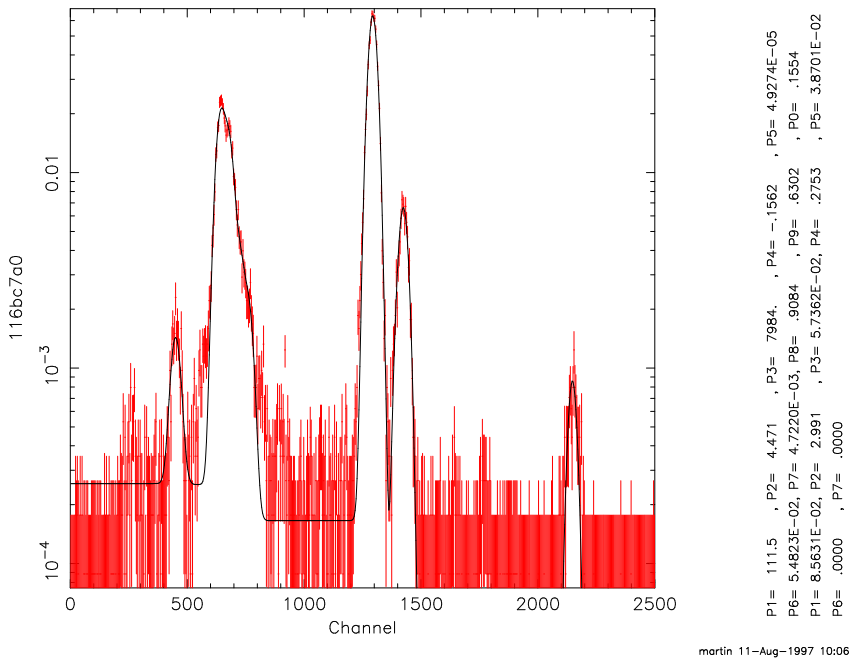

Figure 37: Preliminary results for detected FCM spectrum in amplifier 0 of back-illuminated CCD S3, for ∼1 hr of data taken on Day 116 of calibration at XRCF.

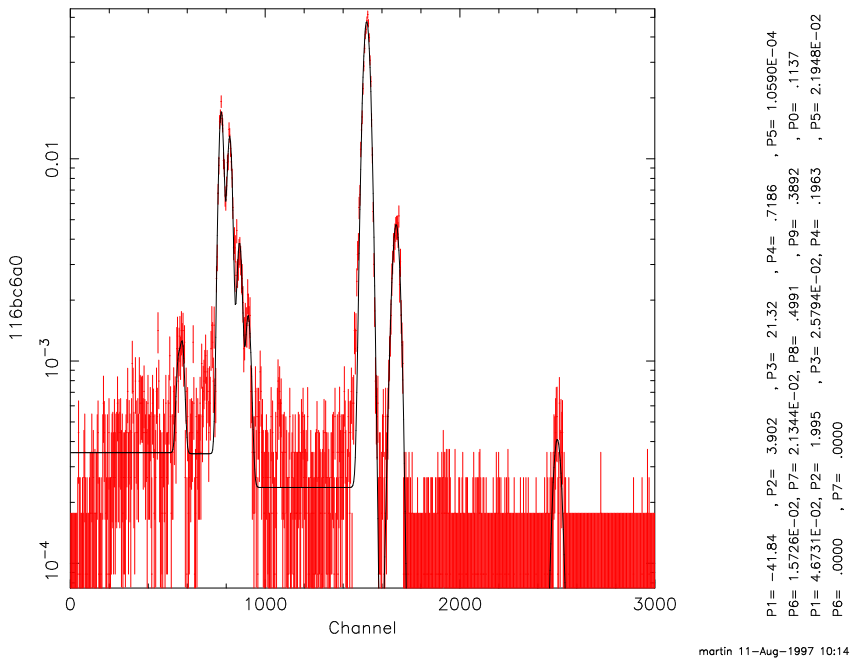

Figure 38: Preliminary results for detected FCM spectrum in amplifier 0 of front-illuminated CCD S2, for ∼1 hr of data taken on Day 116 of calibration at XRCF.

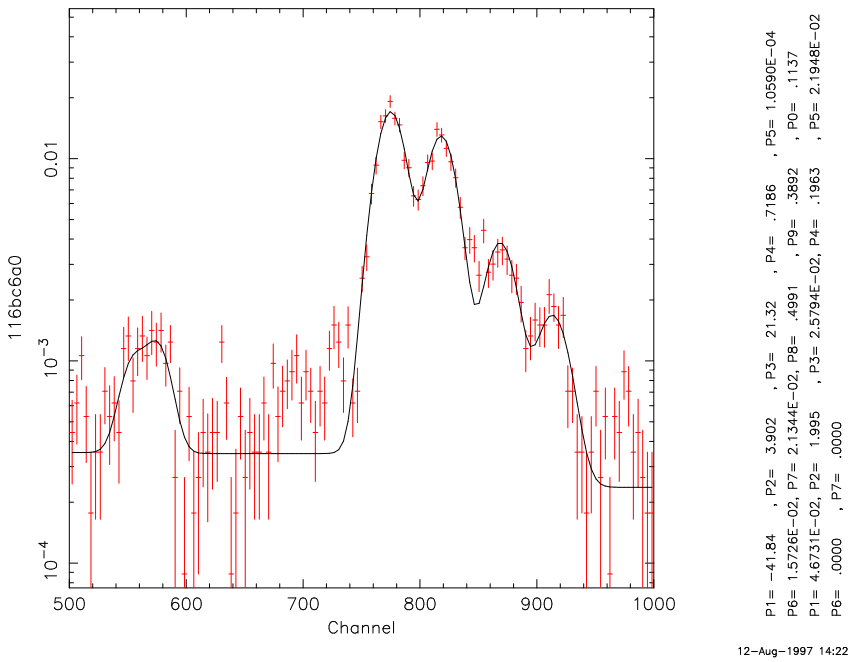

Figure 39: Ag-L line complex region for amplifier 0 of front-illuminated CCD S2, for ∼1 hr of data taken on Day 116 of calibration at XRCF. Note that the modeling does not account for all measured structure.

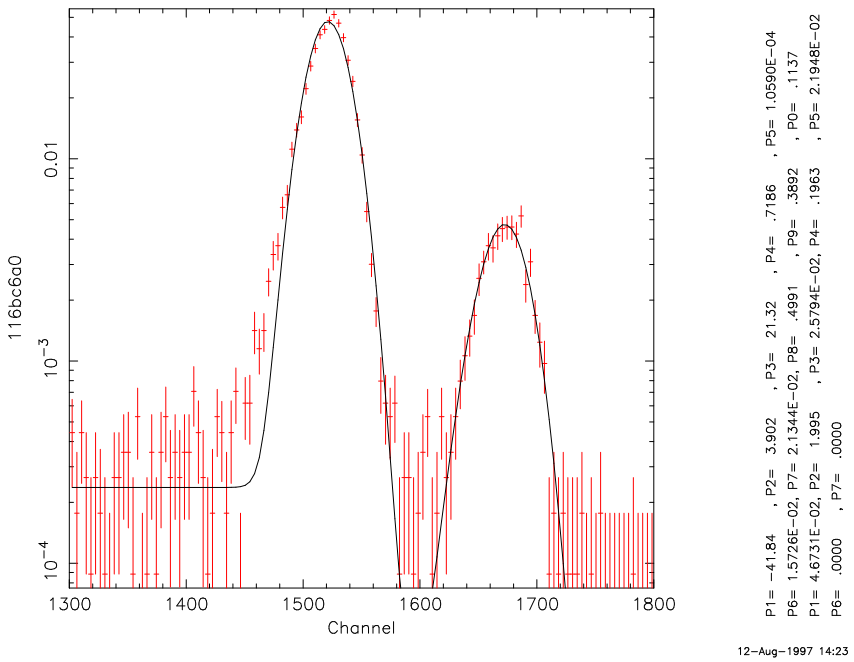

Figure 40: Mn-K line complex region for amplifier 0 of front-illuminated CCD S2 for ∼1 hr of data taken on Day 116 of calibration at XRCF. Note that the modeling does not account for all measured structure.

5.4 Data products

The AXAF Project Science Calibration web page (`wwwastro.msfc.nasa.gov/xray/xraycal/`) will provide links to or instructions for accessing AXAF calibration data products generated by Project Science.

5.4.1 Source characterization

Our web page will provide access to results from the measurement of source activity and the predicted line strengths based upon our simulation.

5.4.2 Forward Contamination Cover (FCC) registration

Our web page will provide access to information on FCC displacements from its nominal position, as determined by centroiding analysis.

5.4.3 Spectral content

Our web page will provide access to information on measured line rates and ratios.

5.4.4 Contamination and flux scale

Our web page will provide access to information on limits on contamination and the flux-scale transfer.

6 Limits on HRMA contamination

6.1 Objectives

The principal objective is to measure or establish upper limits on any contamination of the HRMA mirrors.

6.1.1 Molecular contamination

Molecular contamination can significantly alter the reflectance of grazing-incidence optics [22]. Recognition of this led to stringent control of molecular contamination, resulting in very little molecular-film accumulation on optical witness samples accompanying the HRMA mirrors.

6.1.2 Particulate contamination

Particulate contamination clearly degraded the performance of the AXAF's Verification and Engineering Test Assembly – 1 (VETA-1) [24, 25], primarily by producing more scattered x radiation at lower energies than effected by surface roughness. Realization of this led to stringent control of particulate contamination, resulting in very little accumulation of particulates on optical witness samples accompanying the HRMA mirrors. Consequently, we expect to find little x-ray evidence for dust.

6.2 Procedures

6.2.1 Molecular contamination

The primary x-ray means for detecting a molecular film on the HRMA mirrors are effective-area measurements (e.g., §4.1, [28, 21]). A thin molecular film would increase the HRMA's effective area above the Ir-M_V edge near 2 keV and would produce weak absorption features at energies corresponding to atomic edges of the film's constituent materials.

6.2.2 Particulate contamination

The primary x-ray means for detecting particulates on the HRMA mirrors are to measure the scattering through wing-scan and encircled-energy measurements (e.g., [8]). In addition, shutter-focus and ring-focus measurements (e.g., [26]) provide semi-quantitative information. The energy dependence and the out-of-plane component of the scattering distinguish the effects of dust from those of surface roughness.

6.3 Status

Analyses to measure contamination are derivative to other measurements, as mentioned above. Furthermore, neither the optical witness samples nor the x-ray testing showed any evidence for substantial contamination. Consequently, we have assigned analyses of contamination a low priority.

6.3.1 Molecular contamination

As discussed above, we have assigned a low priority to analyses to bound the molecular contamination. In addition, the current inability of models to account for the observed effective area, to within about 10%, limits our ability to use the effective-area measurements to bound the level molecular contamination.

6.3.2 Particulate contamination

As discussed above, we have assigned a low priority to analyses to bound the particulate contamination.

6.4 Data products

Because this analysis is derivative to other analyses, we or others will have presented the primary data products elsewhere. Data products specific to the analysis of contamination will appear as a brief report, to be linked from the Project Science Calibration web page (`wwwastro.msfc.nasa.gov/xray/xraycal/`).

References

[1] M. C. Weisskopf and S. L. O'Dell, "Calibration of the AXAF observatory: Overview," in *Grazing Incidence and Multilayer X-Ray Optical Systems*, R. B. Hoover and A. B. Walker, eds., *Proc. SPIE* **3113**, pp. 2–17, 1997.

[2] J. J. Kolodziejczak, R. A. Austin, R. F. Elsner, M. K. Joy, M. E. Sulkanen, E. M. Kellogg, and B. J. Wargelin, "X-ray source system at the Marshall Space Flight Center X-Ray Calibration Facility," in *X-Ray and Extreme Ultraviolet Optics*, R. B. Hoover and A. B. Walker, eds., *Proc. SPIE* **2515**, pp. 420–435, 1995.

[3] R. F. Elsner, M. K. Joy, S. L. O'Dell, B. D. Ramsey, and M. C. Weisskopf, "Ground-to-orbit transfer of the AXAF-I flux scale: In-situ contamination monitoring of x-ray telescopes," in *Multilayer and grazing incidence X-ray/EUV optics for astronomy and projection lithography*, R. B. Hoover and A. B. Walker, eds., *Proc. SPIE* **2279**, pp. 332–342, 1994.

[4] B. J. Wargelin, J. P. Hughes, E. M. Kellogg, and T. J. Norton, "Ground calibration of AXAF: The HRMA x-ray detection system," *Bull. Am. Astron. Soc.* **187**, p. 7703, 1995.

[5] W. C. McDermott, E. M. Kellogg, B. J. Wargelin, I. N. Evans, S. A. Vitek, E. Y. Tsiang, D. A. Schwartz, R. Edgar, S. Kraft, F. Scholze, R. Thornagel, G. Ulm, M. Weisskopf, S. O'Dell, A. Tennant, J. Kolodziejczak, and G. Zirnstein, "The AXAF HXDS germanium solid-state-detectors," in *EUV, X-Ray, and Gamma-Ray Instrumentation for Astronomy VIII*, O. H. Siegmund and M. A. Gummin, eds., *Proc. SPIE* **3114**, 1997.

[6] S. Kraft, F. Scholze, R. Thornagel, G. Ulm, W. C. McDermott, and E. M. Kellogg, "High-accuracy calibration of the HXDS hpGe detector at the PTB Radiometry Laboratory at BESSY," in *EUV, X-Ray, and Gamma-Ray Instrumentation for Astronomy VIII*, O. H. Siegmund and M. A. Gummin, eds., *Proc. SPIE* **3114**, 1997.

[7] M. C. Weisskopf, S. L. O'Dell, and L. P. Van Speybroeck, "Advanced X-ray Astrophysics Facility (AXAF): An overview," in *Multilayer and Grazing Incidence X-Ray/EUV Optics III*, R. B. Hoover and A. B. Walker, eds., *Proc. SPIE* **2805**, pp. 2–7, 1996.

[8] L. P. Van Speybroeck, D. Jerius, R. Edgar, T. Gaetz, P. Zhao, and P. Reid, "Performance expectation versus reality," in *Grazing Incidence and Multilayer X-Ray Optical Systems*, R. B. Hoover and A. B. Walker, eds., *Proc. SPIE* **3113**, pp. 89–104, 1997.

[9] S. S.Murray, J. H. Chappell, A. T. Kenter, K. Kobayashi, R. P. Kraft, G. R. Meehan, M. V. Zombeck, G. W. Fraser, J. F. Pearson, J. E. Lees, A. N. Brunton, S. E. Pearce, M. Barbera, A. Collura, and S. Serio, "AXAF high-resolution camera (hrc)," in *EUV, X-Ray, and Gamma-Ray Instrumentation for Astronomy VIII*, O. H. Siegmund and M. A. Gummin, eds., *Proc. SPIE* **3114**, 1997.

[10] E. Y. Tsiang, "JMKmod user manual," *SAO publication* **SAO-AXAF-DR-97-276**, 1997.

[11] K. A. Arnaud, "XSPEC: The first ten years," in *Astronomical Data Analysis Software and Systems*, G. J. V and J. Barnes, eds., *ASP Conference Series* **101**, pp. 17–20, 1996.

[12] B. J. Wargelin, E. M. Kellogg, W. C. McDermott, I. N. Evans, and S. Vitek, "AXAF calibration: the HXDS flow proportional counters," in *Grazing Incidence and Multilayer X-Ray Optical Systems*, R. B. Hoover and A. B. Walker, eds., *Proc. SPIE* **3113**, pp. 526–534, 1997.

[13] E. Y. Tsiang, R. E. Edgar, S. Vitek, and A. F. Tennant, "JMKmod: a software suite within XSPEC for the ground calibration of AXAF," in *Grazing Incidence and Multilayer X-Ray Optical Systems*, R. B. Hoover and A. B. Walker, eds., *Proc. SPIE* **3113**, pp. 132–141, 1997.

[14] R. E. Edgar, E. Y. Tsiang, A. F. Tennant, S. Vitek, and D. A. Swartz, "Spectral fitting in AXAF calibration detectors," in *Grazing Incidence and Multilayer X-Ray Optical Systems*, R. B. Hoover and A. B. Walker, eds., *Proc. SPIE* **3113**, pp. 124–131, 1997.

[15] K. Jahoda and D. McCammon, "Proportional counters as low-energy photon detectors," *Nucl. Inst. Meth.* **A272**, p. 800, 1988.

[16] J. A. Bearden, "X-ray wavelengths," *Rev. Mod. Phys.* **39**, pp. 78–124, 1967.

[17] D. E. Graessle, A. J. Burek, J. J. Fitch, B. Harris, D. A. Schwartz, and R. L. Blake, "Optical constants from synchrotron reflectance measurements of AXAF witness mirrors 2–12 kev," in *Grazing Incidence and Multilayer X-Ray Optical Systems*, R. B. Hoover and A. B. Walker, eds., *Proc. SPIE* **3113**, pp. 52–64, 1997.

[18] D. E. Graessle, J. J. Fitch, B. Harris, P. Hsieh, D. Nguyen, J. Hughes, D. A. Schwartz, and R. L. Blake, "Calibration of AXAF mirrors using synchrotron radiation," *Bull. Am. Astron. Soc.* **187**, p. 7705, 1995.

[19] J. J. Fitch, R. L. Blake, A. J. Burek, A. M. Clark, D. E. Graessle, B. Harris, D. A. Schwartz, and J. Sweeney, "AXAF synchrotron witness mirror calibrations 2–12 kev," in *Grazing Incidence and Multilayer X-Ray Optical Systems*, R. B. Hoover and A. B. Walker, eds., *Proc. SPIE* **3113**, pp. 30–39, 1997.

[20] B. L. Henke, E. M. Gullikson, and J. C. Davis, "X-ray interactions: Photoabsorption, scattering, transmission, and reflection at e = 50–30000 ev, z = 1–92," *Atomic Data & Nuclear Data Tables* **54**, pp. 181–342, 1993.

[21] E. Kellogg, L. Cohen, R. Edgar, I. Evans, M. Freeman, T. Gaetz, D. Jerius, W. C. McDermott, P. McKinnon, S. Murray, W. Podgorski, D. Schwartz, L. Van Speybroeck, B. Wargelin, M. Zombeck, M. Weisskopf, R. Elsner, S. O'Dell, B. Ramsey, A. Tennant, J.Kolodziejczak, G. Garmire, J. Nousek, S. Kraft, F. Scholze, R. Thornagel, G. Ulm, K. Flanagan, D. Dewey, M. Bautz, S. Texter, J. Arenberg, and R. Carlson, "Absolute calibration of the AXAF telescope effective area," in *Grazing Incidence and Multilayer X-Ray Optical Systems*, R. B. Hoover and A. B. Walker, eds., *Proc. SPIE* **3113**, pp. 515–525, 1997.

[22] R. F. Elsner, S. L. O'Dell, and M. C. Weisskopf, "Molecular contamination and the calibration of AXAF," in *Multilayer and grazing incidence X-ray/EUV optics for astronomy and projection lithography*, R. B. Hoover and A. B. Walker, eds., *Proc. SPIE* **1742**, pp. 6–12, 1993.

[23] D. E. Graessle, T. H. Burbine, J. J. Fitch, W. A. Podgorski, J. Z. Juda, R. F. Elsner, S. L. O'Dell, and J. M. Reynolds, "Molecular contamination study of iridium-coated x-ray mirrors," in *Advances in Multilayer and Grazing Incidence X-Ray/EUV/FUV Optics*, R. B. Hoover and A. B. Walker, eds., *Proc. SPIE* **2279**, pp. 12–26, 1994.

[24] J. J. Kolodziejczak, S. L. O'Dell, R. F. Elsner, and M. C. Weisskopf, "Evidence for dust contamination on the VETA-1 mirror surface," in *Multilayer and grazing incidence X-ray/EUV optics for astronomy and projection lithography*, R. B. Hoover and A. B. Walker, eds., *Proc. SPIE* **1742**, pp. 162–170, 1993.

[25] S. L. O'Dell, R. F. Elsner, J. J. Kolodziejczak, M. C. Weisskopf, J. P. Hughes, and L. P. Van Speybroeck, "X-ray evidence for particulate contamination on the AXAF VETA-1 mirrors," in *Multilayer and grazing incidence X-ray/EUV optics for astronomy and projection lithography*, R. B. Hoover and A. B. Walker, eds., *Proc. SPIE* **1742**, pp. 171–182, 1993.

[26] T. J. Gaetz, R. J. Edgar, M. D. Freeman, W. A. Podgorski, L. P. Van Speybroeck, P. Zhao, J. Kolodziejczak, and M. Weisskopf, "Focus and alignment of the AXAF optics," in *Grazing Incidence and Multilayer X-Ray Optical Systems*, R. B. Hoover and A. B. Walker, eds., *Proc. SPIE* **3113**, pp. 77–88, 1997.

[27] E. Browne and R. B. Firestone, *Table of Radioactive Isotopes*, John Wiley and Sons, New York, 1986.

[28] J. J. Kolodziejczak, R. A. Austin, R. F. Elsner, S. L. O'Dell, M. E. Sulkanen, D. A. Swartz, A. F. Tennant, M. C. Weisskopf, G. Zirnstein, and W. C. McDermott, "Uses of continuum radiation in the AXAF calibration," in *Grazing Incidence and Multilayer X-Ray Optical Systems*, R. B. Hoover and A. B. Walker, eds., *Proc. SPIE* **3113**, pp. 65–76, 1997.